

CELL BIOLOGY

Replication-dependent histone labeling dissects the physical properties of euchromatin/heterochromatin in living human cells

Katsuhiko Minami^{1,2}, Kako Nakazato^{1,2}, Satoru Ide^{1,2†}, Kazunari Kaizu^{3,4}, Koichi Higashi^{2,5}, Sachiko Tamura¹, Atsushi Toyoda⁶, Koichi Takahashi³, Ken Kurokawa^{2,5}, Kazuhiro Maeshima^{1,2*}

A string of nucleosomes, where genomic DNA is wrapped around histones, is organized in the cell as chromatin, ranging from euchromatin to heterochromatin, with distinct genome functions. Understanding physical differences between euchromatin and heterochromatin is crucial, yet specific labeling methods in living cells remain limited. Here, we have developed replication-dependent histone (Repli-Histo) labeling to mark nucleosomes in euchromatin and heterochromatin based on DNA replication timing. Using this approach, we investigated local nucleosome motion in the four known chromatin classes, from euchromatin to heterochromatin, of living human and mouse cells. The more euchromatic (earlier-replicated) and more heterochromatic (later-replicated) regions exhibit greater and lesser nucleosome motions, respectively. Notably, the motion profile in each chromatin class persists throughout interphase. Genome chromatin is essentially replicated from regions with greater nucleosome motions, although the replication timing is perturbed. Our findings, combined with computational modeling, suggest that earlier-replicated regions have more accessibility, and local chromatin motion can be a major determinant of genome-wide replication timing.

INTRODUCTION

DNA is wrapped around core histones and forms a nucleosome (1, 2). How are nucleosomes, together with other non-histone proteins/RNAs, organized in the cell as chromatin, and how does chromatin behave in living cells (3, 4)? A wide range of imaging evidence has demonstrated that a string of nucleosomes is rather irregularly folded in the condensed chromatin domains in higher eukaryotic cells (5–12). Genome-wide genomic analyses such as Hi-C (13) also revealed chromatin domains with distinct epigenetic marks (14, 15).

To conduct genome functions, chromatin in the cell is highly variable, ranging from euchromatin to heterochromatin (12, 16–18). A typical textbook model describes euchromatin as open and heterochromatin as closed and condensed (19). However, recent studies suggest that euchromatin domains are not fully open, but rather condensed, except for enhancers and active transcription start sites (8, 10, 12, 20). Given that both euchromatin and heterochromatin form condensed domains, how is heterochromatin physically different from euchromatin? In addition to their histone modifications (e.g., active and inactive ones) and non-histone components [e.g., heterochromatin protein 1 (HP1)] (16–18), their dynamics might also be different (21–24).

Various chromatin labeling and microscopy systems for live-cell imaging and quantitative analyses have been developed to investigate chromatin dynamics and have contributed to understanding

chromatin organization and function in live cells (6, 8, 10, 22–30). Among them, single-nucleosome imaging sensitively and accurately measures local chromatin dynamics in a whole nucleus (24, 31–34) or mitotic chromosomes (24, 35) and provides structural information on how chromatin organizes in living cells. Recently, single-nucleosome imaging revealed that local nucleosome motion (on average) is almost constant throughout interphase (36) and highly constrained during mitosis (24, 35). These local nucleosome motions seem to be mainly driven by thermal fluctuations (36).

Although it is important to understand how heterochromatin is physically different from euchromatin, specific labeling methods for euchromatin and heterochromatin in living cells have been limited (6, 10, 23, 30, 33) and are still challenging, except for specific heterochromatin regions, such as the nuclear periphery and around nucleoli (21, 24, 37). To label euchromatin and heterochromatin specifically in live cells, we have developed a method called replication-dependent histone labeling (Repli-Histo labeling) based on DNA replication timing (38). We investigated local nucleosome motion in the four known chromatin classes from euchromatin to heterochromatin [historically named IA, IB, II, and III (39, 40)] in living human and mouse cells. We reveal that more euchromatic regions have a larger nucleosome motion. The nucleosome motion profile or accessibility of each chromatin class from euchromatin to heterochromatin seems to be maintained throughout interphase. Even when the replication timing program is disrupted, genome chromatin is essentially replicated from regions with higher nucleosome motion. Our methodology and findings dissect physical properties of euchromatin and heterochromatin in live cells, relevant to the stochastic nature of DNA replication initiation.

RESULTS

Development of the Repli-Histo labeling

How can we mark euchromatin/heterochromatin specifically in live human cells? To this aim, we took advantage of DNA replication

Copyright © 2025 The Authors, some rights reserved; exclusive licensee American Association for the Advancement of Science. No claim to original U.S. Government Works. Distributed under a Creative Commons Attribution NonCommercial License 4.0 (CC BY-NC).

¹Genome Dynamics Laboratory, National Institute of Genetics, ROIS, Mishima, Shizuoka 411-8540, Japan. ²Graduate Institute for Advanced Studies, SOKENDAI, Mishima, Shizuoka 411-8540, Japan. ³Laboratory for Biologically Inspired Computing, RIKEN Center for Biosystems Dynamics Research, Kobe, Hyogo 650-0047, Japan. ⁴Cell Modeling and Simulation Group, The Exploratory Research Center on Life and Living Systems, National Institutes of Natural Sciences, Okazaki, Aichi 444-8787, Japan. ⁵Genome Evolution Laboratory, National Institute of Genetics, ROIS, Mishima, Shizuoka 411-8540, Japan. ⁶Comparative Genomics Laboratory, National Institute of Genetics, ROIS, Mishima, Shizuoka 411-8540, Japan.

*Corresponding author. Email: kmaeshim@nig.ac.jp

†Present address: Research Center for Genome & Medical Sciences, Tokyo Metropolitan Institute of Medical Science, Tokyo 156-8506, Japan.

timing, which is a unique feature of eukaryotic DNA replication. Euchromatin replicates in the early S phase, and heterochromatin replicates in the late S phase (Fig. 1A) (38). During this process, newly synthesized histones are provided to the replicated nucleosomes (Fig. 1B). Labeling new histones in the early and late S phases can mark euchromatin and heterochromatin, respectively (Fig. 1C). Based on this concept, we have developed Repli-Histo labeling.

To label nucleosomes, we focused on one of the core histone variants, H3.2, which is expressed in a replication-dependent manner during S phase and incorporated into nucleosomes (41, 42). Once incorporated, H3.2 is stable for hours without exchange (25), allowing us to trace the H3.2 incorporated region. Using the CRISPR-Cas9 system (43), we introduced a HaloTag sequence at the C terminus of endogenous H3.2 genes (Fig. 1D). The HaloTag can be visualized with the HaloTag ligand tetramethylrhodamine (TMR) or other Janelia Fluor (JF) dyes (44). The cell clones stably expressing H3.2-HaloTag (H3.2-Halo) were labeled with TMR and were isolated by fluorescence-activated cell sorting (FACS) (fig. S1A). The proper insertion of the tag sequence and the expression of H3.2-Halo were verified by polymerase chain reaction (PCR) (fig. S1B) and Western blotting (Fig. 1E and fig. S1C). Expressed H3.2-Halo comprises about 20% of the endogenous H3.1/H3.2 (fig. S1C). The distribution of expressed H3.2-Halo

in HeLa cells resembles 4',6-diamidino-2-phenylindole (DAPI) staining ($r = 0.84$; fig. S1D), suggesting that expressed H3.2-Halo is stochastically incorporated into nucleosomes genome wide during the S phase, consistent with the previous reports (41, 45). Stepwise salt washing of nuclei isolated from the H3.2-Halo-expressing cells confirmed that the biochemical behavior of H3.2-Halo is like that of endogenous H3.1/H3.2 (fig. S1E), suggesting that H3.2-Halo was properly incorporated into the nucleosomes in the expressed cells.

For Repli-Histo labeling, we blocked all the existing H3.2-Halo in the cell with nonfluorescent HaloTag ligand, 7-bromo-1-heptanol (7BRO) (46) and inactivated them (Fig. 1F). In S phase cells, the new H3.2-Halo was synthesized and incorporated into new nucleosomes (Fig. 1, F and G) (41, 42, 47). Then, we pulse-labeled the new H3.2-Halo nucleosomes with fluorescent ligands TMR or other JF dyes for 30 min (Fig. 1, F and G). Repli-Histo labelings in the early and late S phases highlight euchromatin and heterochromatin, respectively [Fig. 1H and fig. S1F (right)]. Euchromatic or heterochromatic labeling was judged from its labeling pattern because the replicated chromatin in the nucleus shows unique patterns depending on when the region is replicated [Fig. 1H and fig. S1F (right)] (39, 40). The Repli-Histo signals with H3.2-Halo-TMR were nicely colocalized with nascent DNA pulse labeled with 5-ethynyl-2'-deoxyuridine (EdU) ($r = 0.96$

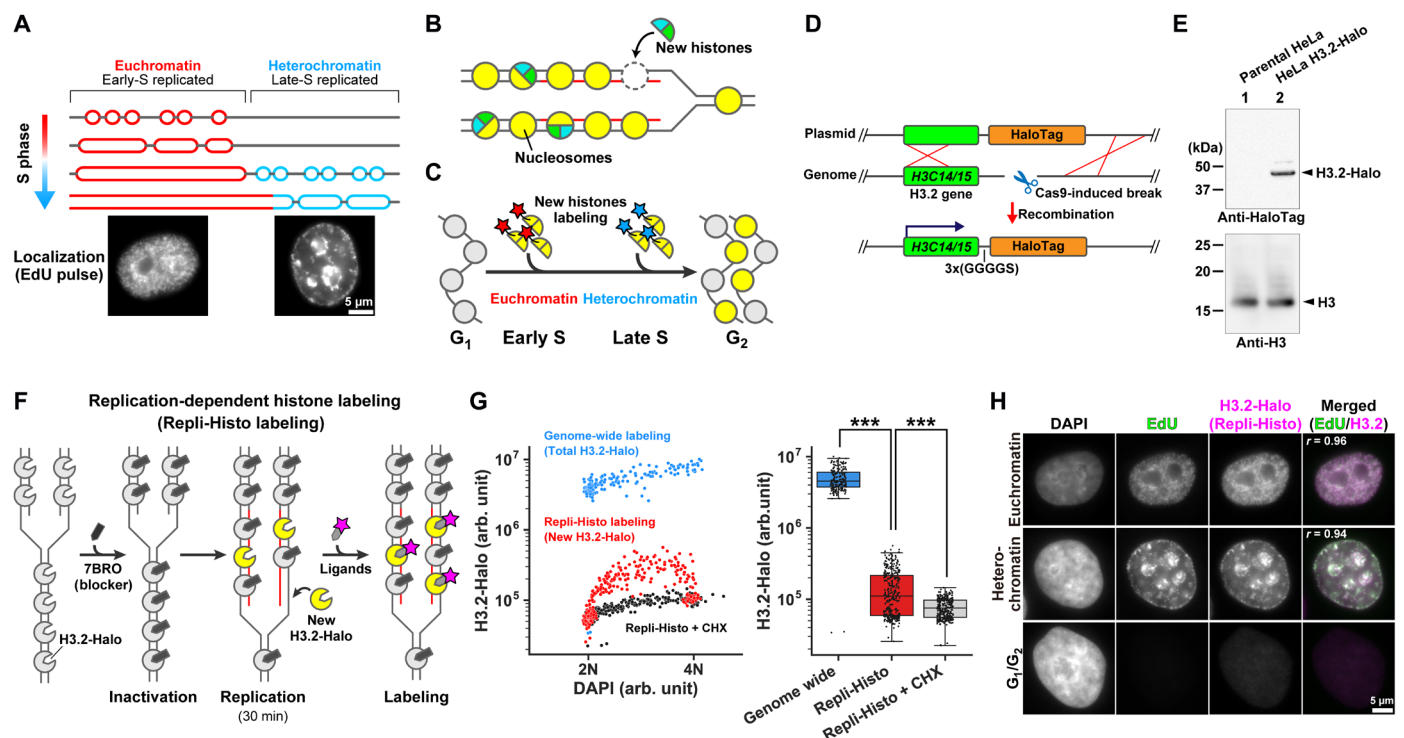


Fig. 1. Development of the Repli-Histo labeling. (A) Eukaryotic cells replicate euchromatin in the early S phase, followed by heterochromatin replication in the late S phase. (B) Newly synthesized histones are incorporated into the replicated nucleosomes. (C) Pulse labeling of the new histones in the early and late S phases allows visualization of euchromatin and heterochromatin, respectively. (D) Schematics of Cas9-mediated HaloTag fusion with endogenous H3.2 genes (H3C14/15). (E) Western blots of H3.2-Halo in lysates of HeLa cells (lane 2) using an anti-HaloTag antibody (top) and an anti-histone H3 antibody (bottom). (F) Schematic of the replication-dependent histone labeling (Repli-Histo labeling). (G) Left: A two-dimensional plot of 4',6-diamidino-2-phenylindole (DAPI) and tetramethylrhodamine (TMR)-labeled H3.2-Halo fluorescence in nuclei. Cyan, genome-wide H3.2-Halo labeling ($n = 192$ cells); red, Repli-Histo labeling ($n = 326$ cells); black, Repli-Histo labeling with cycloheximide (CHX) treatment ($n = 316$ cells). Right: The fluorescent intensity of H3.2-Halo on the left. $***P = 1.9 \times 10^{-77}$ for genome-wide H3.2-Halo and Repli-Histo labeling and $P = 4.62 \times 10^{-15}$ for Repli-Histo labeling and Repli-Histo labeling + CHX by two-sided Mann-Whitney U test. (H) Representative HeLa cells with DAPI staining, EdU pulse labeling, and Repli-Histo labeling. The rightmost column shows the merged image with the Pearson's correlation coefficient (green, EdU–Alexa 488; magenta, Repli-Histo labeling). Top: Euchromatin labeling; middle: heterochromatin labeling; bottom: G_1 – G_2 cell without EdU/Repli-Histo signals.

in euchromatin and $r = 0.94$ in heterochromatin; Fig. 1H). The Repli-Histo signals were abolished by a protein synthesis inhibitor cycloheximide (CHX) (Fig. 1G, black) or a DNA polymerase inhibitor aphidicolin (fig. S1G, black), validating that the Repli-Histo labeling marks only newly synthesized H3.2-Halo in a replication-dependent manner.

Genomic localization of Repli-Histo-labeled nucleosomes

To verify that Repli-Histo labeling specifically marks euchromatin and heterochromatin in live HeLa cells, we determined the genomic localizations of nucleosomes labeled with Repli-Histo labeling (Fig. 2A). We first synchronized HeLa cells at the G₁-S boundary by double thymidine block. After a 1-hour (for euchromatin labeling) or 5-hour

(for heterochromatin) release from the block [Fig. 2A(i)], we inactivated the existing H3.2-Halo with 7BRO and chased for 1 hour with new H3.2-Halo incorporation [Fig. 2A(ii)]. Then, the new H3.2-Halo-nucleosomes from isolated nuclei were conjugated with HaloTag polyethylene glycol (PEG)-biotin ligand [Fig. 2A(iii)]. The nucleosomes with the H3.2-Halo-PEG-biotin were pulled down using streptavidin magnetic beads [Fig. 2A(iv) and fig. S2A]. Nucleosomal DNAs were purified [Fig. 2A(v) and fig. S2B] and subjected to sequencing (Fig. 2B and fig. S2, C and D) as done previously (33).

While peaks of control H2B-Halo nucleosome data (33) and H3.2-Halo without 7BRO treatment were distributed genome wide (fig. S2C), we identified 3750 nucleosome peaks associated with H3.2-Halo of the 1-hour release fraction and 1211 nucleosome

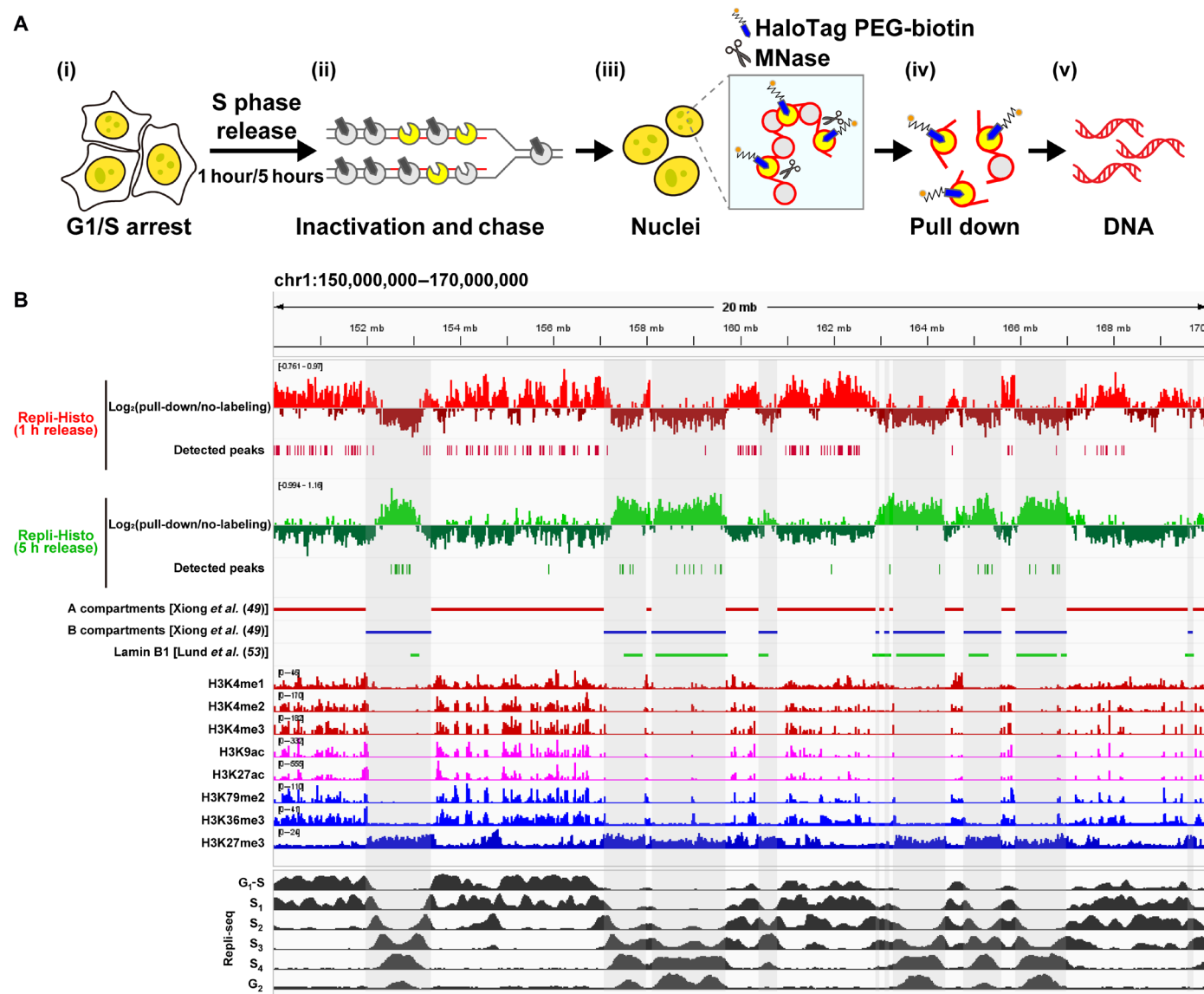


Fig. 2. Genomic localizations of the Repli-Histo-labeled genomic regions. (A) A purification scheme for the Repli-Histo-labeled H3.2-Halo-nucleosomes and their associated genomic DNA. The purified DNA fractions were indexed, amplified, and sequenced. (B) Genomic distribution of the Repli-Histo-labeled H3.2-Halo at 1 and 5 hours after release from double thymidine blocks; view from chr1_150,000,000–170,000,000 (also see fig. S2D for another genomic region). The first and second rows show the labeled H3.2-Halo enrichment relative to a no-labeling control (log₂ ratio) at 10-kb bins. The gray stripes indicate the Hi-C B compartments (49). Previously published data are also shown as indicated on the left.

peaks of the 5-hour release fraction in the annotated HeLa S3 genome (hg19) (Fig. 2B and fig. S2, C and D). The nucleosome peaks of the 1-hour release and 5-hour release fractions are distributed complementary, consistent with the previous Repli-Seq data [(48); <https://doi.org/doi:10.17989%2FENCSR647UES>]. A total of 93.6% of the 1-hour release Repli-Histo fraction belonged to the Hi-C A compartment (15, 49), and 91.8% of the 5-hour release fraction overlapped with the Hi-C B compartment (15, 49). The 1-hour release and 5-hour release Repli-Histo fractions were significantly enriched with active chromatin marks (H3K4me1-3, H3K9ac, H3K27ac, H3K36me3, and H3K79me2) and an inactive chromatin mark (H3K27me3), respectively (fig. S3, A to J) (48, 50), in good agreement with previous Repli-Seq and related studies (51, 52). Consistent with our imaging data (Fig. 1H), the 5-hour release Repli-Histo fraction was associated with lamina-associated domains (45.5% of the fraction; Fig. 2B and figs. S2D and S3K) (53). Together, our genomics analysis indicates that Repli-Histo labeling (1-hour release and 5-hour release fractions) specifically highlights the euchromatin (Hi-C A compartment) and heterochromatin (Hi-C B compartment), respectively.

Single-nucleosome imaging in euchromatin and heterochromatin regions in living cells

Next, we combined Repli-Histo labeling and single-nucleosome imaging (31–33) to measure local nucleosome motion in euchromatin and heterochromatin. We conducted Repli-Histo labeling on asynchronous HeLa cells (Fig. 3A, left). In this case, about 46% of the cells were in the S phase (fig. S1F) and were labeled with Repli-Histo labeling (Fig. 3A, left). Here, we used two colors for the HaloTag ligands: a high concentration of TMR to visualize the labeling patterns and a very low concentration of JF646 (44) to image single nucleosomes (Fig. 3B). After DNA replication, we monitored the nucleosome motion at the G₂ phase (Fig. 3A, right), excluding the possibility that the different DNA content and nuclear size affect the result.

Using oblique illumination microscopy, which allowed us to illuminate a thin area within a single nucleus (Fig. 3A, right) (31, 54), we observed individual nucleosomes in euchromatin and heterochromatin as clear dots and recorded their motions at 50 ms per frame (200 frames, 10 s in total) (Fig. 3B and movies S1 and S2). Each JF646 dot showed a single-step photobleaching (Fig. 3C), while TMR dots did not (fig. S4A), confirming that each JF646 dot represented a single H3.2-Halo-JF646 molecule in a single nucleosome. The individual dots were fitted with a two-dimensional (2D) Gaussian function to estimate the precise position of the nucleosome (55, 56) and were tracked using u-track software (57) to obtain the nucleosome trajectory data (Fig. 3D). The position determination accuracy of fluorescent H3.2-Halo-JF646 dots was 9.5 nm (fig. S4B and see Materials and Methods). We only characterized the behavior of the H3.2-Halo stably incorporated into nucleosomes because the free H3.2-Halo molecules moved too quickly to be tracked with an image acquisition of 50 ms per frame. We also confirmed that 7BRO treatment did not significantly affect nucleosome motion (fig. S4C).

Figure 3B (bottom) displays the heatmaps of nucleosome motions in euchromatin and heterochromatin (more movements show more red, and fewer movements show more blue). From the tracked nucleosome trajectories, we calculated the nucleosome displacement (fig. S4D) and then the mean square displacement (MSD) (Fig. 3E), which shows the spatial extent of motion in a certain time window (fig. S4E). The MSD plots show a subdiffusive curve, and their motions were severely suppressed after chemical fixation with formaldehyde

(FA) (Fig. 3E and movie S3). The plots indicate that nucleosomes in euchromatin are more dynamic than heterochromatin (Fig. 3E and movies S1 and S2), while the control MSD data of H2B-Halo (36) and H3.2-Halo without 7BRO treatment are in the middle of those of euchromatin and heterochromatin (“genome wide” in Fig. 3E and movie S4). The MSD exponent in euchromatic nucleosomes (0.45) is higher than that of heterochromatic nucleosomes (0.34) (Fig. 3E and fig. S4F). Furthermore, we examined the moving angle (motion vector) distribution of individual nucleosomes (Fig. 3F) and calculated the asymmetry coefficient (AC) values (Fig. 3G) (58). Nucleosomes in heterochromatin have more pulling back force (i.e., a smaller AC value; Fig. 3H and fig. S4G) and are more constrained than in euchromatin.

The more-euchromatic regions (earlier-replicated regions) have a larger nucleosome motion

To obtain more information on the nucleosome behaviors in euchromatin and heterochromatin, we categorized whole chromatin into four known classes from euchromatin to heterochromatin based on the replication timing and labeling pattern (Fig. 4A; fig. S5, A to C; movies S5 to S8) (i.e., replication foci; see Table 1 for more details) (39, 40). Historically, the four classified regions were named class IA and class IB, which are earlier-replicated regions (more euchromatic), and class II and class III, which are later-replicated regions (more heterochromatic) (39, 40). Although the cells with the class III pattern have a large amount of freely diffusing H3.2-Halo (Fig. 4A, fig. S5B, and movie S8), we only focused on the behavior of the H3.2-Halo stably incorporated into nucleosomes in the class III pattern (fig. S6A).

Nucleosome motion is progressively more constrained as the class progresses from IA to III (Fig. 4B, fig. S6B, and movies S5 to S8; see also fig. S7). The radius of constraint (R_c ; $p = 6/5 \times R_c^2$, where p is the plateau value of the MSD) of nucleosomes in each class was estimated (mean \pm SD): 132 ± 17 nm (IA), 115 ± 8.6 nm (IB), 105 ± 12 nm (II), and 89 ± 14 nm (III) (fig. S6C). Their MSD exponents α in the time range between 0 and 0.5 s gradually decreased: IA, 0.45; IB, 0.40; II, 0.34; III, 0.25 (Fig. 4B and fig. S6D). Decreases in AC values were also observed (Fig. 4B and fig. S6E): IA, -1.247 ; IB, -1.377 ; II, -1.525 ; III, -1.582 . These data indicate that more euchromatic regions (earlier-replicated regions) have a larger nucleosome motion with higher MSD exponents and AC values. Notably, almost no overlaps or gaps were observed among the four classified regions (Fig. 4, B and C). The nucleosomes around the nuclear periphery [i.e., lamina-associated domains (LADs) (59)] and around nucleoli [nucleolus-associated domains (NADs) (60)] in class II (Fig. 4D) showed similar MSD values (Fig. 4E), suggesting that chromatin replicated at the same time exhibits a similar local nucleosome behavior, regardless of its intranuclear location.

To investigate the generality of the motion profile in euchromatin/heterochromatin (classes IA, IB, II, and III), we tagged the endogenous H3.2 gene in RPE-1 (fig. S8A) and HCT116 cells (fig. S8B) with HaloTag. We also tagged the endogenous H3.1 gene in mouse 10T1/2 fibroblast cells (fig. S8C) (61) to examine pericentromeric heterochromatin foci (chromocenters) (62). Repli-Histo labeling was performed in various stages of their S phase cells (fig. S8, D to F) after validation by PCR and Western blotting (fig. S8, A to C). We observed their nucleosome motions at the G₂ phase. We found a similar motion profile in not only HeLa but also RPE-1, HCT116, and mouse 10T1/2 cells (Fig. 4, F to H, and movies S9 to S12). Nucleosomes in the pericentromeric heterochromatin (chromocenters) behave

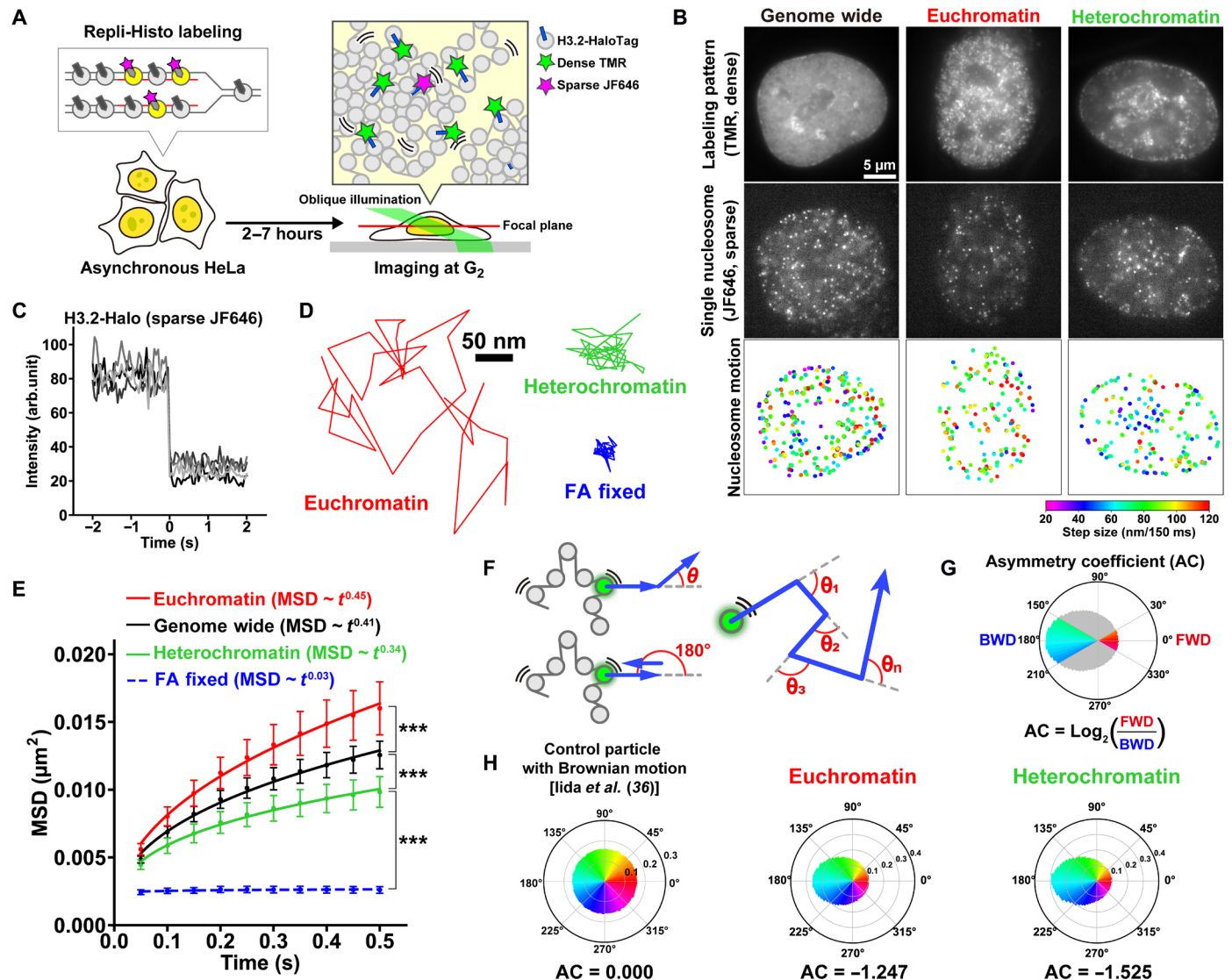


Fig. 3. Euchromatin-/heterochromatin-specific single-nucleosome imaging with Repli-Histo labeling. (A) Schematic of the labeling and imaging. Left: The S phase HeLa cells (~46% of the asynchronous population; fig. S1F) were labeled with Repli-Histo labeling. Right: The Repli-Histo-labeled cells were observed at G₂ phase using oblique illumination microscopy system (31, 54). A small fraction of H3.2-Halo was labeled with JF646 (magenta) for single-nucleosome imaging, and the rest was densely labeled with TMR (green) to visualize labeling patterns. (B) HeLa cells with two-color H3.2-HaloTag labeling. Left: Genome-wide labeling. Center and right: Repli-Histo labeling with euchromatin and heterochromatin patterns. Top: The labeling patterns with dense TMR; middle: single-nucleosomes with sparse JF646; bottom: heatmaps of the single-nucleosome displacement. (C) Single-step photobleaching of five representative nucleosomes (H3.2-Halo-JF646). The horizontal axis shows the time before and after photobleaching. (D) Representative trajectories of tracked single nucleosomes in euchromatin (red) and heterochromatin (green) in live HeLa cells and in formaldehyde (FA)-fixed HeLa cells (blue). (E) MSD plots (\pm SD among cells) of single nucleosomes in euchromatin-labeled (red, $n = 45$), heterochromatin-labeled (green, $n = 36$), and genome-wide-labeled (black, $n = 38$) living HeLa cells from 0.05 to 0.5 s. Blue: MSD from FA-fixed cells ($n = 30$). The plots were fitted as a subdiffusive curve. $***P = 2.0 \times 10^{-16}$ (euchromatin versus genome wide), $P = 7.9 \times 10^{-12}$ (genome wide versus heterochromatin), $P = 3.6 \times 10^{-19}$ (heterochromatin versus FA fixed) by the two-sided Kolmogorov-Smirnov test. (F) Schematic for angle-distribution analysis. (G) Schematic for the asymmetric coefficient (AC) (58). See Materials and Methods for details. (H) Angle distribution from a particle with Brownian motion [left, reproduced from (36)] and nucleosomes in euchromatin-labeled (center, $n = 45$ cells) and heterochromatin-labeled (right, $n = 36$ cells) living HeLa cells. Their AC values are shown at the bottom.

similarly to those of class III in 10T1/2 cells (Fig. 4H). Nucleosomes in the putative inactive X chromosome in RPE-1 cells, which are highly condensed, also seem to belong to class III and are highly constrained (fig. S8D and movie S12). Overall, the more euchromatic regions (earlier-replicated regions) have larger nucleosome motions with higher MSD exponents and AC values (Fig. 4, F to H). The nucleosome motion profiles (MSD exponents and AC values) in

euchromatin/heterochromatin seem to be a general feature in mammalian cells.

The nucleosome motion profile of each chromatin class is maintained throughout interphase

We wondered whether we would see a similar motion profile in the G₁ phase after cell division. To this aim, we arrested the Repli-Histo-labeled

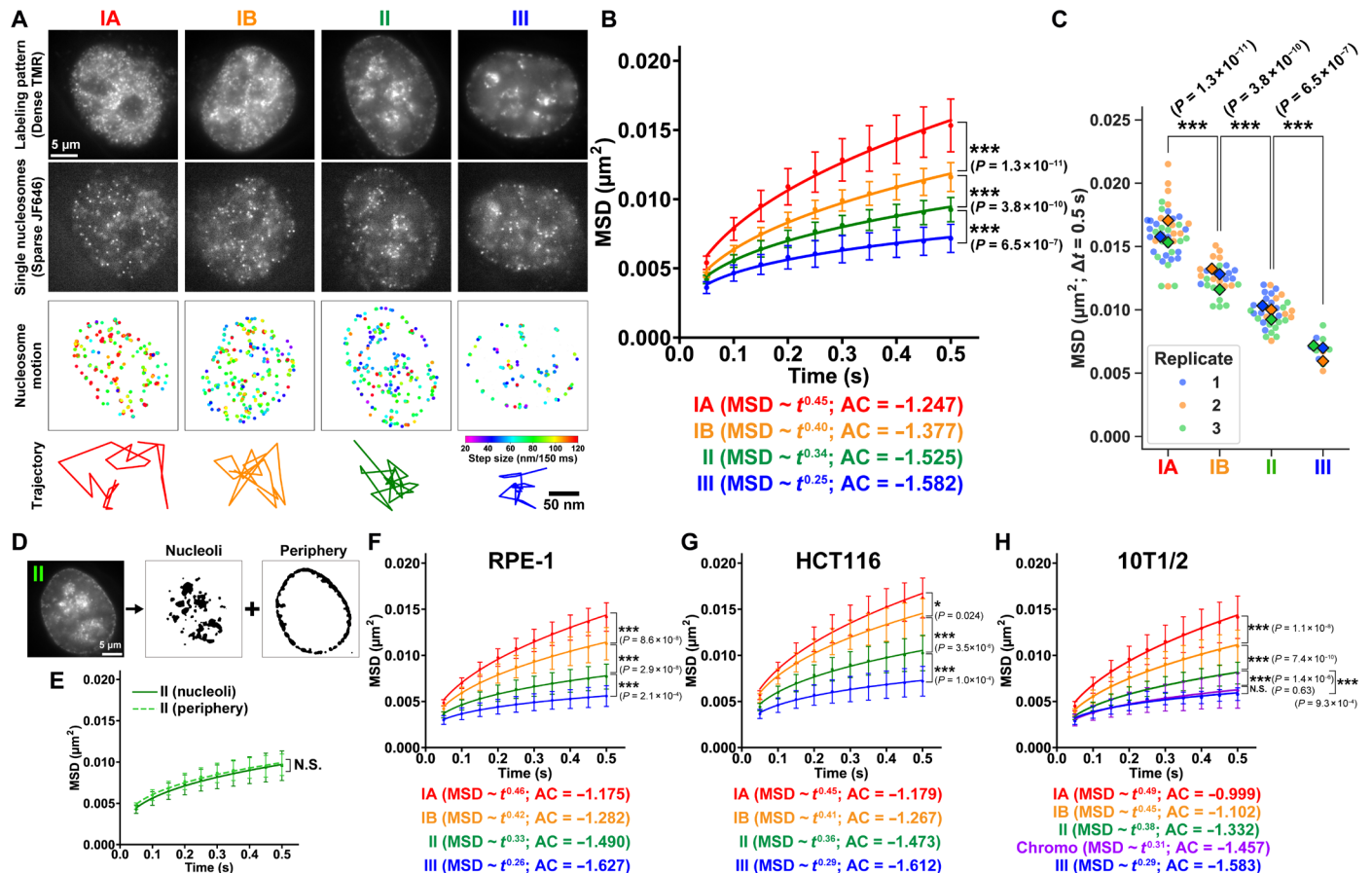
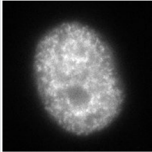
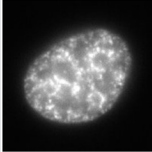
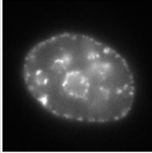
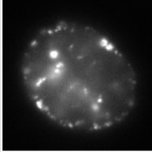
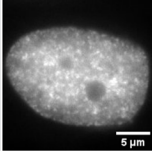


Fig. 4. Local nucleosome movements in the four classes of chromatin regions. (A) HeLa cells with two-color Repli-Histo labeling of the classes IA, IB, II, and III regions. From top to bottom: Labeling patterns (dense TMR), single nucleosomes (sparse JF646), displacement heatmaps, and representative trajectories. (B) MSD plots (\pm SD among cells) of single nucleosomes in IA (red, $n = 45$), IB (orange, $n = 29$), II (green, $n = 36$), and III (blue, $n = 10$) in living HeLa cells. IA and II are reproduced from Fig. 3E (euchromatin and heterochromatin). MSD exponents and the AC values are from fig. S6E. $***P = 1.3 \times 10^{-11}$ (IA versus IB), $P = 3.8 \times 10^{-10}$ (IB versus II), $P = 6.5 \times 10^{-7}$ (II versus III). (C) MSD values at 0.5 s in each cell from (B). Three biological replicates are shown. Diamonds: the mean values in each replicate. (D) Class II chromatin is subcategorized into nucleolus-associated regions (nucleoli) and peri-nuclear regions (periphery). (E) MSD plots (\pm SD among cells) of single nucleosomes in the class II nucleoli region ($n = 22$) and periphery region ($n = 22$). N.S.: $P = 0.87$ by the two-sided Kolmogorov-Smirnov test. (F to H), MSD plots (\pm SD among cells), MSD exponents, and ACs of single nucleosomes in IA (red), IB (orange), II (green), and III (blue) in various cell lines. (F) RPE-1, IA ($n = 36$), IB ($n = 29$), and III ($n = 19$). (G) HCT116, IA ($n = 29$), IB ($n = 21$), II ($n = 22$), and III ($n = 20$). (H) Mouse 10T1/2, IA ($n = 74$), IB ($n = 39$), II ($n = 43$), III ($n = 5$), and chromocenter ($n = 27$). The P values by two-sided Kolmogorov-Smirnov tests are indicated in each panel.

cells at the late- G_1 phase using L-mimosine (Fig. 5A) (63). We found that the Repli-Histo labeling patterns were retained among the G_1 -arrested cells (Fig. 5B), consistent with previous reports that replication foci patterns are retained throughout several cell cycles (64). Again, the R_c , MSD exponents, and AC values all gradually decreased as class progressed from IA through III (Fig. 5C; fig. S9, A and B; and movies S13 to S16). The nucleosome motion profile of each chromatin class (IA, IB, II, and III) was maintained between the G_1 and G_2 phases. This finding is consistent with our previous data, which shows that the average motion of nucleosomes labeled by H2B-Halo in the G_1 and G_2 phases is very similar (36).

Next, we questioned whether the nucleosome motion profile of each chromatin class is also maintained throughout the S phase. A significant fraction of the H3.2-Halo in the cells with the class III pattern diffused freely (movie S8 and fig. S5B), and this fraction disturbed the observation at the subsequent S phase. We thus fused HaloTag to the C terminus of endogenous CDC45, the component

of active DNA helicase, which stably binds to the replicating chromatin region (65), to generate HeLa cells expressing endogenous CDC45-HaloTag (Fig. 6A). We confirmed that all endogenous CDC45 alleles were tagged with HaloTag (Figs. 6B and fig. S10, A and B) in a clone, which proliferated normally (fig. S10C), confirming that the CDC45-Halo is functional. While the labeled CDC45-Halo was diffusive in the G_1/G_2 phase (second row in Fig. 6C and movie S17), CDC45-Halo formed several specific foci patterns during the S phase (second row in Fig. 6C), which were analogous to those of the EdU-labeled nascent DNA (replication foci), depending on the replication timing (third row in Fig. 6C) (66). They correspond to classes IA, IB, II, and III. We performed single-molecule imaging of CDC45-Halo stably bound fractions (Fig. 6D and movies S18 to S21) to track the local behaviors of active replication sites in the various S phase stages. Observed MSD values of CDC45-Halo throughout the S phase stages were akin to those of single nucleosomes in corresponding classes IA, IB, II, and III in the G_2 phase

Table 1. Description of the labeling pattern in each class.			
Class	Replication timing*	Image†	Labeling pattern
IA	~2 hours after the S-phase onset		Throughout the nucleoplasm, excluded from the nuclear and nucleolar periphery
IB	~4 hours after the S-phase onset		Throughout the nucleus, including the nuclear and nucleolar periphery
II	~6 hours after the S-phase onset		Nuclear and nucleolar periphery
III‡	~7 hours after the S-phase onset		Large and discrete dot-like foci at the nucleoplasm and periphery
Ambiguous (Fig. 9 and fig. S13)	Appears in RIF1-depleted cells with aberrant replication timing		Not categorized into any of the four classes, and distributed uniformly throughout the nucleus
*Replication timing was determined by cell cycle–synchronized HeLa cells. †Scale bar, 5 μm. ‡Class III H3.2-Halo also shows diffusive signals that are not colocalized with nascent DNA with EdU incorporation (fig. S5B).			

(Fig. 6D and fig. S10, D and E). We concluded that the local motion profile of each chromatin class is maintained throughout interphase, even where DNA replication is ongoing.

Repli-Histo labeling dissects physical properties of euchromatin and heterochromatin in live human cells

To further investigate the physical natures of euchromatin and heterochromatin using Repli-Histo labeling, we focused on the distances between two nucleosomes in close proximity and examined the mean-squared distance between them (two-point MSD) (Fig. 7A) (10, 67) because the distance between nucleosomes is much less affected by either translational or rotational movements of the chromatin domain during imaging. We performed Repli-Histo labeling with a very low concentration of TMR and JF646 and tracked two spatially neighboring single nucleosomes. Cell cycle synchronization allowed the labeling of euchromatic (IA) and heterochromatic (II) domains (fig. S5C and see also Materials and Methods). Single nucleosomes labeled with TMR and JF646 were imaged using a beam splitter system (Fig. 7B and fig. S11A).

We simultaneously observed clear dots in each color channel [Fig. 7C and movie S22; position determination accuracy was 11.2 nm (TMR) and 10.9 nm (JF646) in fig. S11B]. Note that there was essentially no cross-talk between the TMR and JF646 signals (fig. S11, C and D). Among them, we found many pairs of nucleosomes with TMR and JF646 signals located in close proximity [Fig. 7C (insets) and movie S23]. We collected nucleosome pairs whose distance is less than 150 nm (Fig. 7A and movies S22 and S24), which are likely in the same chromatin domain (10), and analyzed their motions. Two-point MSD plots showed rather subdiffusive curves (Fig. 7D), suggesting that nucleosomes fluctuate inside the chromatin domain like a liquid. This fluctuation was severely suppressed after the chemical fixation with FA [Fig. 7D (dashed lines) and movies S25 to S26]. The nucleosome pairs in euchromatin domains showed larger two-point MSD than in heterochromatin domains (Fig. 7D, red and green solid lines). Two-point MSD plots using Repli-Histo labeling suggest that nucleosomes inside the euchromatin domain fluctuate more than those in the heterochromatin domain (Fig. 7E). Nucleosomes in heterochromatin are more constrained and seem closer to a gel-like state, presumably due to more crosslinks such as HP1 (16–18).

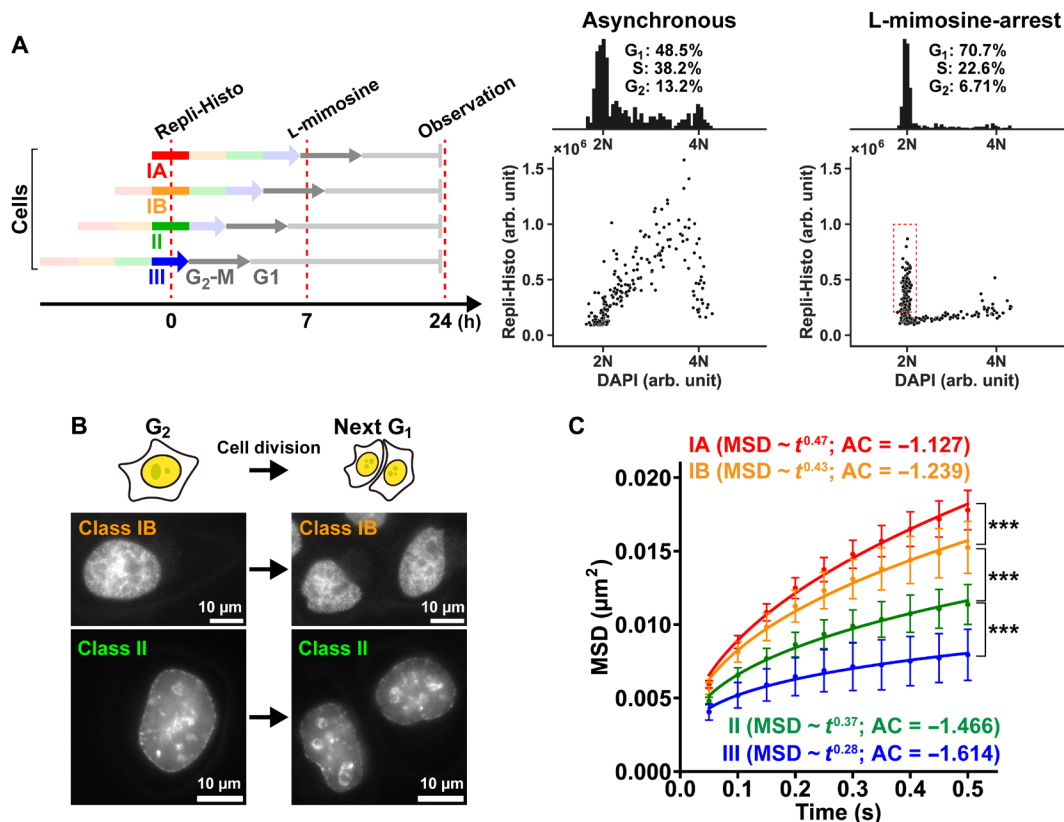


Fig. 5. The nucleosome motion profile of each chromatin class in the G₁ phase. (A) Left: Schematics of the G₁ synchronization using L-mimosine. Right: Two-dimensional plots of DAPI and Repli-Histo–labeled H3.2-Halo fluorescence in asynchronous and L-mimosine–treated HeLa cells. The top shows the histograms of the DAPI intensity indicating cell cycle profiles. The cell cycle profiles were estimated by the Dean-Jett-Fox method. Most of the Repli-Histo–labeled cells are arrested at the G₁ phase (red rectangle) in L-mimosine–treated cells. (B) Time-lapse imaging of HeLa cells with Repli-Histo labeling. The Repli-Histo labeling patterns are retained among the G₁ cells after cell division. (C) MSD plots (\pm SD among cells) of single nucleosomes in classes IA (red, $n = 37$), IB (orange, $n = 18$), II (green, $n = 15$), and III (blue, $n = 10$) in G₁-arrested living HeLa cells from 0.05 to 0.5 s. MSD exponents and the AC values from fig. S9 are also shown in the brackets. *** $P = 4.5 \times 10^{-6}$ for class IA versus IB, $P = 2.4 \times 10^{-4}$ for class IB versus II, and $P = 4.6 \times 10^{-5}$ for class II versus III by the two-sided Kolmogorov-Smirnov test.

Local nucleosome motion facilitates chromatin accessibility to large proteins

Our findings using Repli-Histo labeling revealed that genome chromatin is primarily replicated from regions with greater nucleosome motions (Fig. 4, B and F to H). We hypothesized that local nucleosome fluctuation governs chromatin accessibility to a limited number of replication initiation factors to fire replication origins (Fig. 8A) (68, 69).

To tackle this hypothesis, we reconstructed the chromatin environment in silico using the Metropolis Monte Carlo method (70) to simulate what fraction of macromolecules can penetrate the chromatin domain with fluctuating nucleosomes. The model nucleosomes were placed on one side of the simulation space (“chromatin domain”) at 0.5 mM (Fig. 8B). The nucleosomes in the domain are mobile with defined radius of fluctuation (R_f) (71–73). We put model diffusing proteins (tracers) in the uncrowded space and examined how many diffusing proteins access the core region of the chromatin domain (see Materials and Methods for details). This simple model might not necessarily reflect the chromatin state in live cells because the mimic nucleosome spheres are not connected by linker DNA. However, they are still useful for testing our hypothesis.

Although small tracers (<10 nm) freely moved in the crowded chromatin domains regardless of nucleosome R_f [Fig. 8C (top) and

movies S27 and S28], large tracers (>10 nm), which correspond to replication initiation complexes/factors (74, 75), could not reach the core region of the chromatin domains with immobile nucleosomes [Fig. 8C (bottom) and movie S29], consistent with previous reports that local nucleosome fluctuation increased the accessibility to large proteins (movie S30) (71–73). The tracer penetration depends both on the R_f of nucleosomes and the tracer diameter (Fig. 8D). This suggests that the nucleosome motion affects the kinetics of the tracer (i.e., model protein) penetration. The larger the nucleosome fluctuates, the faster the model protein can penetrate the chromatin domain (Fig. 8, D and E). In particular, the model proteins with a 20-nm diameter, which correspond to replication initiation complexes/factors (74, 75), penetrated only the chromatin domain with nucleosome fluctuation (Fig. 8, D and E). In our modeling, we did not consider the entropy effect, but larger objects would tend to be entropically excluded from chromatin domains in the cell, which might further enhance the differences in Fig. 8 (D and E).

Depletion of RIF1 coordinately affects local chromatin motion and DNA replication timing

Last, we wondered whether the genome-wide landscape of local chromatin motion (Fig. 8A) contributes to the regulation of DNA

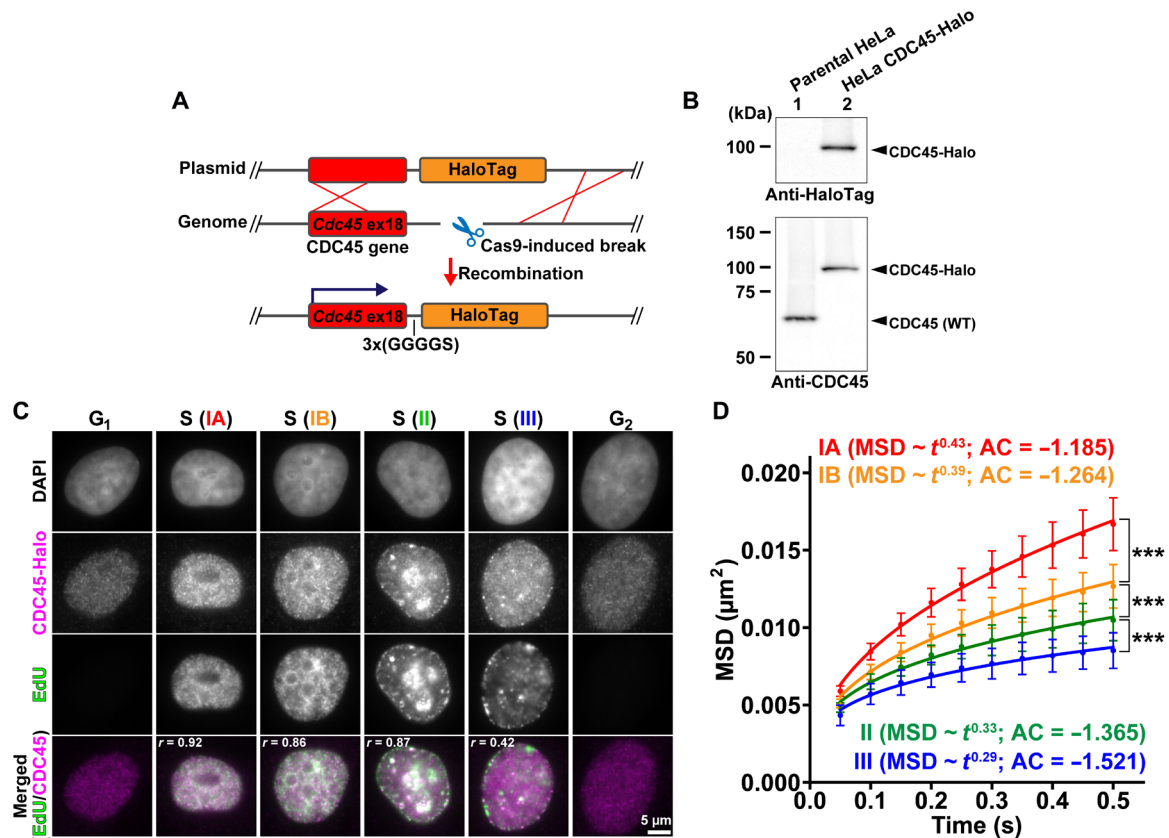


Fig. 6. Single-CDC45 imaging reveals the nucleosome motion profile during the S phase. (A) Schematics of Cas9-mediated HaloTag fusion with the endogenous CDC45 gene (Cdc45). (B) Western blots of CDC45-Halo in lysates of HeLa cells using an anti-HaloTag antibody (top) and an anti-CDC45 antibody (bottom). Lane 1: Parental HeLa cells; lane 2: HeLa cells expressing endogenous CDC45-Halo. (C) HeLa cells with CDC45-Halo–labeled with JF646 (second row) and EdU-pulse labeling (third row). Chromatin classes (IA, IB, II, and III) were categorized as described in Table 1. The bottom row shows the merged image of EdU (green) and CDC45-Halo (magenta) with their corresponding Pearson's correlation coefficients. (D) MSD plots (\pm SD among cells) of single CDC45-Halo with classes IA (red, $n = 41$), IB (orange, $n = 15$), II (green, $n = 23$), and III (blue, $n = 24$) patterns in living HeLa cells from 0.05 to 0.5 s. MSD exponents and the AC values from fig. S10 (D and E) are also shown in the brackets. *** $P = 1.2 \times 10^{-5}$ for class IA versus class IB; $P = 7.7 \times 10^{-4}$ for class IB versus class II; $P = 2.0 \times 10^{-5}$ for class II versus class III by the two-sided Kolmogorov-Smirnov test.

replication timing. To address this question, we perturbed the genome-wide replication program by knocking down one of the key replication timing regulators, RIF1 (fig. S13, A and B) (76, 77). The depletion of RIF1 perturbs the replication timing by increasing cell-to-cell heterogeneity of the replication timing (78). Consistent with the previous study (78), 40% of cells with RIF1 knockdown by small interfering RNA (siRNA) showed an “ambiguous Repli-Histo labeling pattern,” which could not be categorized into the four classes, ensuring effective perturbation of the replication timing (Table 1 and fig. S13C).

For single-nucleosome imaging in RIF1 knockdown cells, we first prelabeled the existing H3.2-Halo with Rhodamine 110 Direct (R110) (Fig. 9A) so that the total intensity of R110 could identify the S phase stage (or replication timing) in the cell (first row, Fig. 9B). We then performed Repli-Histo labeling for the newly replicated nucleosomes with dual color (Fig. 9A and movie S31): a high concentration of TMR to visualize the Repli-Histo labeling patterns and a very low concentration of JF646 to image single nucleosomes (second and third rows, Fig. 9B). After DNA replication, we monitored the nucleosome motion at the following G₂ phase (Fig. 9, C and D).

The control cells with mock depletion exhibited a clear anticorrelation between local nucleosome motion and DNA contents (i.e.,

S phase stage in the labeling or replication timing) (Fig. 9E; Spearman's correlation coefficient $\rho = -0.67$). The earlier-replicated regions have a larger nucleosome motion with higher MSD exponents and AC values (Fig. 9C and fig. S13, D and E). Strikingly, this anticorrelation was also retained in the RIF1-depleted cells ($\rho = -0.57$; Fig. 9F), suggesting that genome chromatin is essentially replicated from regions with greater nucleosome motions, although the genomic replication timing program is perturbed.

The RIF1 depletion slightly up-regulated the average local nucleosome motion (fig. S13F), indicating that RIF1 somehow constrains the local nucleosome motions in specific chromatin regions or whole chromatin. Which chromatin regions are constrained by RIF1? It is likely that the class II chromatin region is constrained by RIF1 because of the following reasons. First, class II chromatin was reduced after RIF1 depletion (fig. S13C). RIF1 seems to constrain the local nucleosome motion of class II (mid-S replicating) chromatin and maintain its mid-replication (Fig. 9, E and F, bottom). Consistently, RIF1 localization is similar to class II chromatin (second to third rows in fig. S13A), as reported previously (76, 77). Second, chromatin with the ambiguous Repli-Histo patterns upon RIF1 depletion showed a similar nucleosome motion and replication timing to the class IB chromatin (“ambiguous,” Fig. 9, C and D).

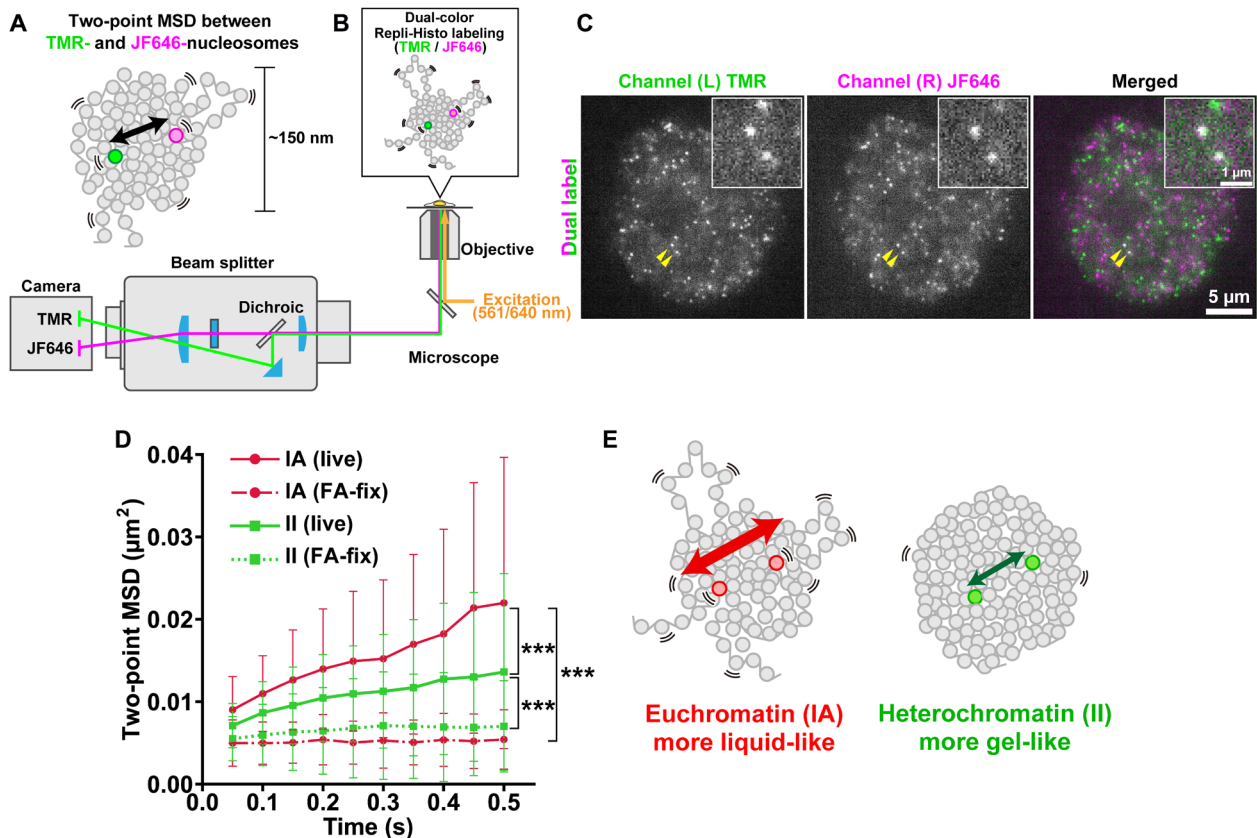


Fig. 7. Two-point MSD analysis to dissect the physical properties of euchromatin and heterochromatin. (A) Schematic for two-point MSD analysis. The mean square relative distances between the TMR and JF646 nucleosomes were tracked. The neighboring dot pairs whose averaged distances were <150 nm were analyzed. (B) Schematic for dual-color imaging with a beam splitter system (W-VIEW GEMINI, Hamamatsu Photonics). The images of two single nucleosomes with different colors were simultaneously acquired with a single sCMOS. (C) Representative images of single-nucleosomes simultaneously labeled with TMR (left) and JF646 (center) by Repli-Histo labeling in living HeLa cells. Right: The merged image. The two pairs of nucleosomes in close proximity (yellow arrowheads) are enlarged (inset). See also movie S23. (D) Two-point MSD plots (mean ± SD among dot pairs) between TMR and JF646 nucleosomes in HeLa cells with indicated conditions: Repli-Histo labeling with class IA pattern in live cells (red solid line, $n = 48$ pairs); class IA pattern in FA-fixed cells (red dashed line, $n = 63$ pairs); class II pattern in live cells (green solid line, $n = 168$ pairs); class II pattern in FA-fixed cells (green dashed line, $n = 140$ pairs). *** $P = 6.7 \times 10^{-4}$ for class IA (live) versus class II (live), $P = 7.4 \times 10^{-17}$ for class IA (live) versus IA (FA fixed), and $P = 1.5 \times 10^{-11}$ for class II (live) versus II (FA fixed) by the two-sided Kolmogorov-Smirnov test. (E) Schematic of how euchromatin behaves more liquid-like with larger nucleosome fluctuation inside the condensed chromatin domain than heterochromatin.

Together, our results suggest that RIF1 knockdown diminishes the constraints of mid-replicating chromatin, up-regulates its nucleosome motion, and facilitates the earlier replication of the regions. Again, this finding supports the notion that genome chromatin is primarily replicated from regions with greater nucleosome motions (Fig. 8A).

DISCUSSION

To specifically label euchromatin and heterochromatin in living mammalian cells, we have developed Repli-Histo labeling in this study. Repli-Histo labeling allows chromatin visualization of the four regions (classes IA, IB, II, and III; Fig. 4A) historically categorized based on replication timing (39, 40). We have quantitatively measured nucleosome motion in these four chromatin regions at a high spatiotemporal resolution, which had yet to be conducted. We have demonstrated that the more euchromatic regions have larger local chromatin motion, and the heterochromatic regions are more constrained (Fig. 4, B and C). The nucleosomes in the heterochromatin around the nuclear periphery and

nucleoli showed similar MSD values (Fig. 4E), suggesting that chromatin replicated at the same timing exhibits similar physical properties, regardless of its intranuclear location. Two-point MSD analyses of two neighboring nucleosome distances suggested the fluidity of their chromatin domains. Euchromatin looks more liquid-like, and heterochromatin is more gel-like, presumably due to additional crosslinks in heterochromatin such as HP1 and lamina (Fig. 7, D and E) (16–18, 59). Because local chromatin motion can facilitate chromatin accessibility to large proteins, greater motion in euchromatin empowers transcription competency while both types of chromatin retain a certain degree of accessibility (Fig. 8A). Our findings shed light on the physical nature of euchromatin and heterochromatin.

Our data also show that chromatin cannot be bimodally classified into euchromatin and heterochromatin. Since the nucleosome motion is increasingly more constrained as the class progresses from IA through III, chromatin exhibits a rather continuous chromatin-state spectrum. This concept is in good agreement with the Hi-C subcompartment idea (15) and “chromatin color” formed by multiple combinations of the chromatin modifications (52, 79).

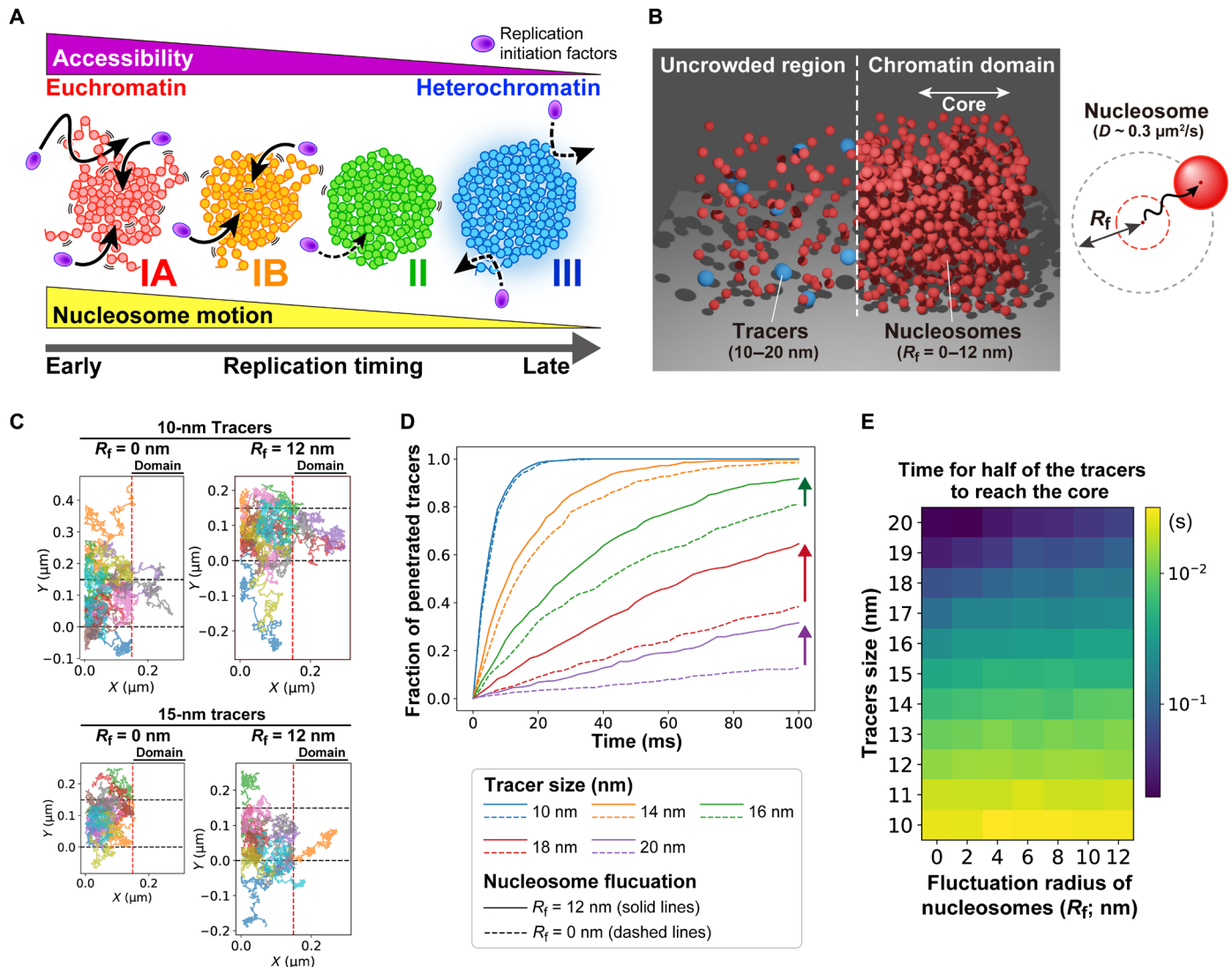


Fig. 8. Local nucleosome motion facilitates accessibility of condensed chromatin domains. (A) Model illustrating how the landscape of local nucleosome motion from euchromatin (early-replicated) to heterochromatin (late-replicated) can govern the chromatin accessibility to rate-limiting replication initiation factors, which determines the probability of origin firing. (B) Left: Schematic of the reconstructed chromatin environment in silico by the Monte Carlo simulation. The model diffusion proteins (tracer; blue) are initially put in the left uncrowded space. The model nucleosomes (red) are placed on the right (“chromatin domain”) with a defined nucleosome fluctuation radius (R_f). Right: Scheme for fluctuation radius (R_f) of the model nucleosomes. An experimentally estimated diffusion coefficient of nucleosomes ($D \sim 0.3 \mu\text{m}^2/\text{s}$) was used (for details, see fig. S12). (C) Representative ($n = 10$) trajectories of the tracers during 1 ms of the simulation. The tracer diameters and the nucleosome R_f s are shown on the top. Red dashed lines denote the boundary of chromatin domains; black dashed lines denote the periodic boundary of the reconstructed environment. (D) Fractions of the tracers with various diameters that penetrated the core region of the chromatin domain with various nucleosome R_f s. Note that the penetration rates of large tracers are facilitated by nucleosome fluctuation (arrows). (E) Time it takes for half of the tracers to reach the core of the chromatin domain. Simulations with various tracer diameters and nucleosome R_f s were conducted.

In contrast to the motion difference between different chromatin classes (IA, IB, II, and III), the chromatin motion in each class is maintained constant throughout the G_1 , S, and G_2 phases (Figs. 4B, 5C, and 6D). This finding is consistent with our previous genome-wide observation (36) showing that the local chromatin motion, on average, remains constant throughout interphase. Because the constant chromatin motion allows cells to conduct housekeeping functions (e.g., transcription and DNA replication) under similar environments throughout interphase, cells can do their routines in each genome chromatin region under a similar condition during interphase. The

constant chromatin motion in each chromatin class also maintains the reactivity preference among the classes, including euchromatin and heterochromatin, during interphase. Our finding that the chromatin motion in each class is similar between the S phase and G_1/G_2 phases is consistent with our previous report that the rapid degradation of MCM2 by the AID system (i.e., disassembly of the DNA replisome) did not significantly affect local chromatin motion (36). This implies that DNA replication complexes, such as the replisome, do not actively induce nucleosome motions, at least on the second timescale.

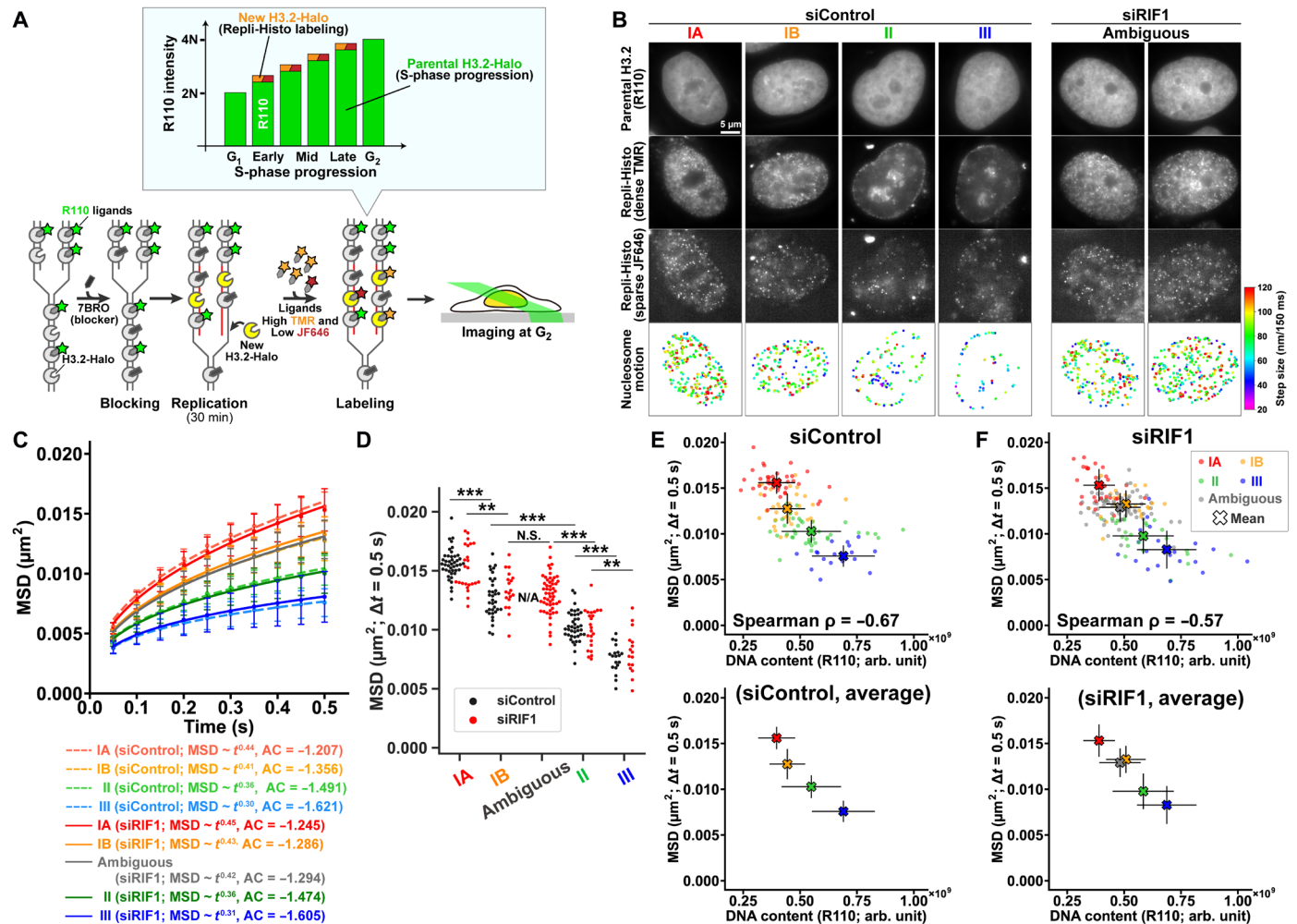


Fig. 9. RIF1 depletion coordinately affects local nucleosome motion and DNA replication timing. (A) Three-color Repli-Histo labeling. Parental H3.2-Halo was labeled with green R110 direct ligands, identifying the S phase progression or replication timing (top). The remaining H3.2-Halo were blocked with 7BRO, followed by TMR/JF646 pulse labeling. (B) Representative control (siControl) and RIF1-depleted (siRIF1) HeLa cells with the three-color Repli-Histo labeling. First row: Parental H3.2-Halo (R110); second and third rows: the Repli-Histo labeling patterns (TMR; see also Table 1) and corresponding single nucleosomes (JF646); fourth row: displacement heatmaps. (C) MSD plots (\pm SD among cells) of single nucleosomes in IA (siControl, $n = 43$; siRIF1, $n = 27$), IB (siControl, $n = 35$; siRIF1, $n = 22$), II (siControl, $n = 40$; siRIF1, $n = 24$), III (siControl, $n = 19$; siRIF1, $n = 23$), and ambiguous patterns (siRIF1, $n = 72$) in siControl (dashed lines) or siRIF1 (solid lines) cells from 0.05 to 0.5 s. MSD exponents and AC values are from Fig. S13 (D and E). (D) MSD at 0.5 s in each cell from (C). For siControl, $***P = 5.6 \times 10^{-10}$ (IA versus IB), $P = 1.9 \times 10^{-8}$ (IB versus II), and $P = 1.6 \times 10^{-8}$ (II versus III). For siRIF1, $**P = 0.0012$ (IA versus IB), $P = 0.0035$ (II versus III), and $***P = 5.7 \times 10^{-10}$ ("ambiguous" vs. II). $**P = 3.2 \times 10^{-9}$ (IB versus II). N.S.: $P = 0.70$ (IB versus "ambiguous"). Data are tested by the two-sided Kolmogorov-Smirnov test. N/A, not applicable ($n = 0$). (E and F) Correlation between MSD at $t = 0.5$ s [from (D)] and R110 intensity (reflecting DNA content at the time of Repli-Histo labeling) in control (siControl) (E) and RIF1-depleted (siRIF1) (F) HeLa cells. Spearman's correlation coefficients are shown. The bold "X" and bars represent each stage's mean and SD (also indicated at the bottom).

Our present study provides a possible physiological role of the chromatin motion landscape in DNA replication timing. We propose that local nucleosome fluctuation is a stochastic factor in replication timing that determines the origin firing efficiency of a given genomic region (Fig. 8A) for the following reasons. First, multiple studies have demonstrated that eukaryotic replication origins fire stochastically with a certain probability (80–82), supporting the stochastic nature of replication timing (83). Second, several studies have reported that limited numbers of initiation factor(s), such as SLDs and CDC45, are competed for among origins during the firing process (68, 69). With greater nucleosome motions, initiation factors bind to the origins more efficiently (Fig. 8, D and E). Consistently, almost no overlaps or gaps between the MSD plots in the four

class regions were observed (Fig. 4, B and C and F to H). On the other hand, the process of DNA replication elongation does not appear to be affected by differences in nucleosome motion between the four class regions, as CDC45 foci (representing active replication helicase) were detected even in the heterochromatic class III chromatin (Fig. 6C).

Then, if we up-regulate the nucleosome fluctuation of a certain region, does the region replicate earlier in the S phase? Yes. First, as we showed in this study, the knockdown of RIF1 seems to increase nucleosome motion in class II regions (mid-S replicating) and facilitates earlier replication of the regions (Fig. 9, E and F, bottom). Second, histone deacetylase (HDAC) inhibitor treatment, which up-regulates nucleosome motions globally (6, 10), shifts the replication

timing of chromocenter heterochromatin earlier (84). Numerous studies have reported that many factors—including trans-acting factors such as RIF1, histone modifications, and spatial organization (78, 85–88)—can affect the replication timing. In addition to the RIF1–protein phosphatase 1 (PP1) axis counteracting the Dbf4-dependent kinase (DDK)–mediated origin activation (89), these factors may govern nucleosome fluctuation and chromatin accessibility to the rate-limiting replication initiation factors for origin firing (Fig. 8A) (68, 69). Nonetheless, our findings do not exclude the possibility that replication timing is determined by an unknown factor that also affects nucleosome mobility. Further investigation is needed.

Last, it would be valuable to explore potential applications of Repli-Histo labeling technology. Because our Repli-Histo labeling and imaging on the euchromatic and heterochromatic regions were conducted at conventional microscopic resolution, super-resolution live-cell imaging techniques such as photoactivated localization microscopy (PALM) (55) or 3D structured illumination microscopy (3D-SIM) (8) could provide even more detailed insights. These methods would enable the examination of how macromolecules, such as proteins and RNAs, reach their target sites, as suggested in (9). Another promising application is the use of correlative light and electron microscopy (CLEM), which combines the global contrast and high resolution of electron microscopy with the molecular specificity of fluorescence microscopy (90). The integration of these techniques now offers a closer match in resolution between the two modalities, light and electron microscopy, allowing specific euchromatin and heterochromatin to be visualized at nanoscale resolution in the context of the crowded intracellular environment (91).

MATERIALS AND METHODS

Plasmid construction

Construction of pX330-H3.2-gRNA (guide RNA), pX330-CDC45-HaloTag, and pX330-H3.1-gRNA was carried out as described previously (92). Gene-specific guide RNA sequences for human histone H3.2 (*H3C14/H3C15*), CDC45 (*CDC45*), and mouse histone H3.1 (*Hist1h3a*) genes were designed using the CRISPR design website (CHOPCHOP (93)) and inserted into the BbsI cloning site in pX330 (#42230, Addgene), as previously described (43). The guide RNA sequence was 5'-CCGCCGCATCCGTGGAGAGC-3' for H3.2, 5'-GAACCCCTGTAACTCACCCCT-3' for CDC45, and 5'-ACAAT-TAGCCCTCTCCCCG-3' for mouse H3.1.

The construction of donor plasmids pGEM-H3.2-HaloTag, pGEM-CDC45-HaloTag, and pGEM-H3.1-HaloTag was carried out as follows. The HaloTag coding sequence was PCR-amplified using KOD FX (KFX-101, Toyobo) from the pFC14A HaloTag CMV Flexi Vector (G965A, Promega). The homology arms for human H3.2, CDC45, and mouse H3.1 flanked from the HaloTag sequence [~700 base pair (bp) each] were PCR-amplified from HeLaS3 and 10T1/2 genomic DNA, which was isolated using a Wizard Genomic DNA Purification kit (Promega). The homology arms and the HaloTag fragment were inserted between the EcoRI and SalI sites of the pGEM-T (Easy) vector (A137A, Promega) using the In-Fusion HD Cloning Kit (639648, Clontech).

Cell lines

HeLaS3, RPE-1, and 10T1/2 (61) (a gift from M. J. Hendzel at University of Alberta) cells were cultured at 37°C in 5% CO₂ in Dulbecco's modified Eagle's medium (DMEM) (D5796- 500ML, Sigma-Aldrich)

supplemented with 10% fetal bovine serum (F7524, Sigma-Aldrich). HCT116 cells were gifted from M. T. Kanemaki (National Institute of Genetics, Mishima, Japan) and were cultured at 37°C in 5% CO₂ in McCoy's 5A medium (SH30200.01, HyClone) supplemented with 10% fetal bovine serum. The HeLaS3 cell line stably expressing H2B-Halo was previously established as described in (6).

To establish HeLaS3, RPE-1, and HCT116 cells expressing endogenous human H3.2 or CDC45 tagged with HaloTag, a CRISPR-Cas9 genome editing system was used. The constructed plasmid pGEM-H3.2-HaloTag or pGEM-CDC45-HaloTag as well as the Cas9/sgRNA expression plasmid pX330-H3.2-gRNA or pX330-CDC45-gRNA were electroporated into the HeLaS3, RPE-1, or HCT116 cells. The electroporation was performed using the Neon Transfection System (Invitrogen). After 1 to 2 weeks, the cells expressing H3.2-HaloTag or CDC45-HaloTag were fluorescently labeled with 50 nM HaloTag TMR ligand (G8252, Promega) or JF646 ligand (GA1120, Promega) overnight at 37°C in 5% CO₂. The HaloTag TMR ligand-positive cells were then collected using flow cytometry (SH800S, Sony Biotechnology). The collected cells were subcloned, and the cells stably expressing H3.2-HaloTag or CDC45-HaloTag were selected. The selected clones were rechecked with PCR for correct insertion of the HaloTag coding sequence downstream of the endogenous H3.2/CDC45 loci. To establish 10T1/2 cells expressing endogenous mouse H3.1 tagged with HaloTag, a similar CRISPR-Cas9 genome editing was performed as follows. The constructed plasmids pGEM-H3.1-HaloTag and pX330-H3.1-gRNA were electroporated into the 10T1/2 cells using the Neon Transfection System (Invitrogen). The 10T1/2 clone stably expressing mouse H3.1-HaloTag was selected as described above. The selected clone was rechecked with PCR for correct insertion of the HaloTag coding sequence downstream of the endogenous H3.1 locus.

RNA interference

siRNA transfection was performed using Lipofectamine RNAiMAX (13778-075, Thermo Fisher Scientific) according to the manufacturer's instructions. The transfected cells were used for subsequent studies 48 h after transfection. The siRNA oligonucleotide targeting RIF1 sequence (Invitrogen; sense: 5'-GAAUGAGCCCCU-AGGGAAATT-3') (94) was used. A control oligonucleotide (4390843, Thermo Fisher Scientific) was used for mock depletion.

Western blotting

Cells were lysed in Laemmli sample buffer supplemented with 10% 2-mercaptoethanol (133-1457, Wako) and incubated at 95°C for 5 min to denature proteins. The cell lysates, equivalent to 1 × 10⁵ cells per well, were subjected to SDS–polyacrylamide gel electrophoresis (SDS-PAGE) (12.5% for histone detection and 8% for CDC45 detection). For Western blotting, the fractionated proteins in the gel were transferred to a polyvinylidene difluoride (PVDF) membrane (IPVH00010, Millipore) by a semi-dry blotter (BE-320, BIO CRAFT). After blocking with 5% skim milk (190-12865, Fujifilm Wako), the membrane-bound proteins were probed by the rabbit anti-H3 (1:25,000; ab1791, Abcam), mouse anti-H3.1/H3.2 (1:1000; CEC-006; Cosmo Bio), mouse anti-HaloTag (1:1000; G9281, Promega), or rabbit anti-CDC45 (1:1000; 11881S, Cell Signaling Technology), followed by the appropriate secondary antibody: anti-rabbit immunoglobulin G (IgG) (1:5000; 170-6515; Bio-Rad) or anti-mouse IgG (1:5000; 170-6516; Bio-Rad) horseradish peroxidase–conjugated goat antibody. Bands were detected by chemiluminescence reactions

(WBKLS0100, Millipore), and images were acquired with the EZ-Capture MG (AE-9300H-CSP, ATTO).

Biochemical fractionation of nuclei from cells expressing H3.2-HaloTag

Nuclei were isolated from HeLa cells expressing endogenous H3.2-HaloTag as described previously (36). Briefly, collected cells were suspended in nuclei isolation buffer [3.75 mM tris-HCl (pH 7.5), 20 mM KCl, 0.5 mM EDTA, 0.05 mM spermine, 0.125 mM spermidine, aprotinin (1 μ g/ml) (T010A, TaKaRa), and 0.1 mM phenylmethylsulfonyl fluoride (PMSF) (P7626-1G, Sigma-Aldrich)] and centrifuged at 1936g for 7 min at room temperature. The cell pellets were resuspended in nuclei isolation buffer and again centrifuged at 1936g for 7 min at room temperature. Subsequent steps were performed at 4°C unless otherwise noted. Cell pellets were resuspended in nuclei isolation buffer containing 0.025% Empigen (45165-50ML, Sigma-Aldrich) (nuclei isolation buffer+) and homogenized immediately with 10 downward strokes of a tight Dounce pestle (357546, Wheaton). The cell lysates were centrifuged at 4336g for 5 min. The nuclear pellets were washed in nuclei isolation buffer+. The nuclei were incubated on ice for 15 min in the following buffers containing various concentrations of salt: Hepes-EDTA (HE) buffer [10 mM Hepes-NaOH (pH 7.5), 1 mM EDTA, and 0.1 mM PMSF], HE + 100 mM NaCl, HE + 500 mM NaCl, HE + 1 M NaCl, and HE + 2 M NaCl. After each buffer incubation with increasing concentrations of salt, centrifugation was performed to separate the nuclear suspensions into supernatant and pellet fractions. The proteins in the supernatant fractions were precipitated by using 17% trichloroacetic acid (208-08081, Wako) and cold acetone. Both pellets were suspended in a Laemmli sample buffer and subjected to 12.5% SDS-PAGE, followed by Coomassie brilliant blue (031-17922; Wako) staining and Western blotting using rabbit anti-H3 (ab1791, Abcam) and rabbit anti-HaloTag (G9281, Promega) antibodies to confirm H3.2-HaloTag expression.

HaloTag labeling

To check the distribution of the expressed HaloTag-fused proteins, H3.2-Halo or CDC45-Halo were fluorescently labeled with 50 nM HaloTag TMR or JF646 ligands overnight at 37°C in 5% CO₂. Subsequently, the cells were fixed with 1.85% FA (064-00406, Wako) for 15 min and then permeabilized with 0.5% Triton X-100 (T-9284, Sigma Aldrich) for 5 min and stained with DAPI (0.5 μ g/ml; 10236276001, Roche) for 5 min before embedded in paraphenylene diamine (PPDI) [20 mM Hepes (pH 7.4), 1 mM MgCl₂, 100 mM KCl, 78% glycerol, and PPDI (1 mg/ml; 695106-1G, Sigma-Aldrich)].

For single-nucleosome imaging, H2B-Halo, H3.2-Halo, and H3.1-Halo molecules were fluorescently labeled with 50 pM HaloTag TMR ligand for 20 min at 37°C in 5% CO₂. The cells were washed with Hank's balanced salt solution (HBSS) (1× HBSS, H1387; Sigma-Aldrich) three times and then incubated in a phenol red-free DMEM (21063-029, Thermo Fisher Scientific) or McCoy's 5A (1-18F23-1, BioConcept) for over 2 hours before live-cell imaging.

For single-CDC45 imaging, CDC45-Halo in asynchronous HeLa cells was fluorescently labeled with 5 nM HaloTag JF646 ligand for 30 min at 37°C in 5% CO₂, followed by labeling with 10 nM HaloTag TMR ligand overnight. The cells were then washed with 1× HBSS three times and then incubated in a medium without phenol red for more than 4 hours before live-cell imaging. We observed the S phase

cells, which formed CDC45-Halo foci corresponding to classes IA, IB, II, and III (movies S18 to S21).

Repli-Histo labeling

The Repli-Histo labeling was performed as follows. First, asynchronous cells expressing endogenous H3.2-HaloTag were incubated with the medium supplemented with 10 μ M 7BRO (B1852; Tokyo Chemical Industry) (46) for 60 min at 37°C in 5% CO₂. The cells were then washed three times with medium without 7BRO. The Repli-Histo labeling with 10T1/2 cells expressing mouse H3.1-Halo was performed similarly.

For fixed cell imaging, the cells were exposed to the medium supplemented with 100 nM HaloTag TMR ligand and 10 μ M EdU (C10337, Thermo Fisher Scientific) for 30 min immediately after washing out 7BRO. For negative control, CHX (100 μ g/ml; 037-20991, Fujifilm Wako) or aphidicolin (5 μ g/ml; A0781, Sigma-Aldrich) were also added to inhibit the new H3.2-Halo synthesis or DNA replication, respectively. The cells were then fixed and permeabilized as described above. Subsequently, EdU was labeled with Alexa Fluor 488 or 647 azide using the Click-iT EdU Cell Proliferation Kit (C10337, Thermo Fisher Scientific) and stained with DAPI (0.5 μ g/ml) for 5 min before being embedded in PPDI as described above.

For fig. S5B, the soluble H3.2-Halo was pre-extracted with 0.5% Triton X-100 in ice-cold CSK buffer [10 mM Hepes-KOH (pH 7.5), 300 mM sucrose, 100 mM NaCl, 3 mM MgCl₂, 1× cComplete Mini protease inhibitor cocktail (11836153001, Roche) and 0.1 mM PMSF (P7626, Sigma-Aldrich)] for 2 min and washed with the same ice-cold buffer without Triton X-100 (twice for 3 min). Subsequent operations were carried out as described above.

For single-nucleosome imaging, the cells were exposed to the mixture of 2 nM HaloTag TMR ligand and 5 nM HaloTag JF646 ligand for 30 min. The cells were then washed three times with a medium without phenol red, followed by incubation in a medium without phenol red for 1 hour before live-cell imaging.

For Fig. 9, the parental H3.2-HaloTag was labeled with 10 nM HaloTag R110Direct ligands (G3221, Promega) overnight before the blocking with 7BRO. The following Repli-Histo labeling for single-nucleosome imaging was carried out as described above.

To characterize the replication timing of the labeled regions, the labeled patterns (historically called replication foci) of the Repli-Histo labeling were manually categorized into the four classes (IA, IB, II, and III) based on previous studies (see Table 1) (39). Alternatively, the replication timing of the Repli-Histo-labeled region was estimated from the total nuclear pixel intensities [arbitrary units (arb. unit)] of R110Direct-labeled parental H3.2-HaloTag (Fig. 9A).

Cell cycle synchronization

To obtain HeLa cells arrested in the late G₁ phase, asynchronous HeLa cells were first labeled with the Repli-Histo labeling, chased for 7 hours, and then treated with 400 μ M L-mimosine (M0253-25MG, Sigma-Aldrich) for 17 hours (Fig. 5A) (63). For cell cycle synchronization of HeLa cells in the early/late S phase, double thymidine block and release were performed as follows. HeLa cells (1.0×10^5 cells) were plated with 3 mM thymidine (T9250, Sigma-Aldrich) for 18 hours, released into a thymidine-free medium for 9 hours, and again treated with 3 mM thymidine for 17 hours for the G₁/S arrest. The arrested cells were then released into a thymidine-free medium for 1 hour (class IA), 3 hours (class IB), 5 hours (class II), or 6 hours (class III).

HaloTag pull-down sequencing

Cell nuclei were isolated as previously described (33) with minor modifications. First, we arrested HeLa cells at G₁-S by double thymidine block treatment as described above. The cells were next released into the S phase for 1 or 5 hours, followed by 10 nM 7BRO treatment for 30 min. After a three-time wash of 7BRO with PBS, the cells were incubated with a 7BRO-free medium for 1 hour for the deposition of newly synthesized H3.2-Halo. The cells were then collected and washed with nuclei isolation buffer [3.75 mM tris-HCl (pH 7.5), 20 mM KCl, 0.5 mM EDTA, 0.05 mM spermine, 0.125 mM spermidine, 0.1% Trasylol (14716, Cayman Chemical), and 0.1 mM PMSF (P7626-1G, Sigma-Aldrich)] by two cycles of centrifugal spins at 193g for 7 min at 23°C. The pellets were then resuspended in nuclei isolation buffer containing 0.05% Empigen BB detergent (45165-50ML, Sigma-Aldrich) (nuclei isolation buffer+) and immediately homogenized with 10 downward strokes using a tight Dounce pestle. After a 5-min centrifugation of the cell lysates at 440g, the pellets were washed and resuspended in nuclei isolation buffer+. After another centrifugation at 440g at 4°C for 5 min, the supernatant was removed and resuspended in 10 ml of nuclei isolation buffer+. This step was repeated four times before the samples were ready for nucleosome purification.

Chromatin purification was carried out as described by (33, 91), with some modifications. The nuclei (equivalent to ~2 mg of DNA) in nuclei isolation buffer [10 mM tris-HCl (pH 7.5), 1.5 mM MgCl₂, 1.0 mM CaCl₂, 0.25 M sucrose, and 0.1 mM PMSF] were digested with 50 U of micrococcal nuclease (MNase) (LS004797, Worthington) at 30°C for 1 hour. In this digestion step, 5 μ M HaloTag PEG-biotin ligand (G859A, Promega) or an equivalent amount of dimethyl sulfoxide (DMSO) was added. After centrifugation at 440g at 4°C for 5 min, the nuclei were lysed with lysis buffer [10 mM tris-HCl (pH 8.0), 5 mM EDTA, and 0.1 mM PMSF] on ice for 5 min. The lysate was dialyzed against dialysis buffer [10 mM Hepes-NaOH (pH 7.5), 0.1 mM EDTA, and 0.1 mM PMSF] at 4°C overnight using Slide-A-Lyzer (66380, Thermo Fisher Scientific). The dialyzed lysate was centrifuged at 20,400g at 4°C for 10 min. The supernatant was recovered and used as the purified nucleosome fraction (mainly mono nucleosomes). To verify complete micrococcal nuclease digestion, DNA was purified, electrophoresed on a 1.5% agarose gel, and visualized by staining with ethidium bromide (fig. S2B).

The biotinylated or untreated nucleosome fraction (28 μ g) was diluted with an equal volume of 2 \times binding buffer [10 mM Hepes-NaOH (pH 7.5), 200 mM NaCl, 2 mM dithiothreitol (DTT), and cComplete EDTA-free protease inhibitor cocktail (11873580001, Roche)]. As shown previously (95), the chromatin solution was added to streptavidin-FG beads (TAS8848 N1170, Tamagawa-Seiki) pre-equilibrated with coating buffer [PBS, 2.5% bovine serum albumin, and 0.05% Tween 20] for 1 hour. The mixtures were incubated at 5°C for 2 hour on a shaker. The beads were collected with a magnetic rack and subjected to the washing procedure as described by Gatto *et al.* (47). Briefly, the beads were washed once with 1 ml of cold 1 \times binding buffer [10 mM Hepes-NaOH (pH 7.5), 100 mM NaCl, and 1 mM DTT], twice with 1 ml of cold wash buffer 1 [Hepes-NaOH (pH 7.5), 140 mM NaCl, 1% Triton X-100, 0.5% NP-40 substitute (11332473001, Roche), and 0.1% SDS], twice with 1 ml of cold wash buffer 2 [Hepes-NaOH (pH 7.5), 360 mM NaCl, 1% Triton X-100, 0.5% NP-40, and 0.1% SDS], twice with 1 ml of cold wash buffer 3 [Hepes-NaOH (pH 7.5), 250 mM LiCl, 0.5% Triton X-100,

and 0.5% NP-40], and once with TE buffer [10 mM tris-HCl (pH 8.0) and 1 mM EDTA]. Beads were resuspended in 50 μ l of TE buffer.

For DNA extraction, 40 μ l of beads underwent ribonuclease (RNase) digestion [4 μ l of RNase A (10109169001, Roche), 1 mg/ml, 30 min at 37°C] and subsequent proteinase K digestion in the presence of SDS [4 μ l of proteinase K (20 mg/ml; 169-21041; Wako) and 10 μ l of 10% SDS, at 1200 rpm and 50°C on shaker for 1 hour]. Beads were removed by magnetic separation and DNA extracted using AMPure XP beads (A63880, Beckman Coulter) according to the manufacturer's instructions and eluted in Milli-Q water. The total DNA content of each sample was measured using Qubit system (Q32851, Thermo Fisher Scientific), and the quality of DNA samples was assessed by an Agilent 2100 Bioanalyzer using an Agilent High Sensitivity DNA kit (5067-4626, Agilent). cDNA libraries were synthesized by the ThruPLEX DNA-seq Kit (R400675, Takara). The size distributions of the libraries were checked by an Agilent 2100 Bioanalyzer using an Agilent High Sensitivity DNA kit. The pooled amplicon library was sequenced with paired-end 2 \times 100 bp reads on the Illumina NovaSeq 6000 platform.

For protein analysis of the HaloTag pull-down fraction (fig. S2A), the remaining 10 μ l of beads was resuspended with an equal volume of 2 \times Laemmli sample buffer supplemented with 10% 2-mercaptoethanol (133-1457, Wako) and incubated at 95°C for 10 min. Beads were removed by centrifugation at 10,000g for 3 min. The input sample and the pull-down samples from the biotinylated and untreated nucleosome (negative control) were separated using SDS-PAGE and were subjected to Western blotting with anti-HaloTag antibody (G9211, Promega).

For data analysis of purified H3.2-Halo-labeled nucleosomal DNA, the nf-core (96) chromatin immunoprecipitation sequencing (ChIP-seq) pipeline (nfcore/chipseq: version 2.0.0) was utilized using a Docker configuration profile and executed using the default parameters. The human genome hg19, retrieved from Illumina's iGenomes, was used for the reference genome. Peaks were detected using the broad mode of MACS2 (97). To evaluate the overlap between the H3.2-HaloTag-labeled regions and contact domains (i.e., Hi-C A/B compartment and histone modification patterns), we compared the H3.2-HaloTag regions with previously published data as described in (10, 33). Compartment annotations on the HeLa cell genome are SNIPER predictions obtained from (49). Peak lists on hg19 genome defined by the ChIP-seq analysis for the histone modifications were obtained from the ENCODE portal (48, 98) with the following identifiers: H3K4me2 (ENCFF108DAJ), H3K4me3 (ENCFF447CLK), H3K9ac (ENCFF723WDR), H3K27ac (ENCFF144EOJ), H3K79me2 (ENCFF916VLX), H3K36me3 (ENCFF001SVY), H3K4me1 (ENCFF162RSB), and H3K27me3 (ENCFF252BLX). Peak lists on hg19 genome defined by ChIP-seq analysis for the lamin B1 were obtained from (53) (Gene Expression Omnibus accession number: GSE57149). The Repli-Seq profiles of HeLa cells were obtained from the ENCODE portal (ENCSR647UES).

Indirect immunofluorescence

Immunostaining was performed as described previously (71), and all processes were performed at room temperature. Cells were fixed in 1.85% FA in PBS for 15 min and then treated with 50 mM glycine in HMK [20 mM Hepes (pH 7.5) with 1 mM MgCl₂ and 100 mM KCl] for 5 min and permeabilized with 0.5% Triton X-100 in HMK for 5 min. After washing twice with HMK for 5 min, the cells were incubated with 10% normal goat serum (NGS; 143-06561, Wako) in

HMK for 30 min. The cells were incubated with the diluted primary antibody, rabbit anti-RIF1 (1:1000; A300-568A, Bethyl Laboratories), in 1% NGS in HMK for 1 hour. After being washed with HMK four times, the cells were incubated with the diluted secondary antibody, goat anti-rabbit IgG Alexa Fluor 488 (1:500; A11006, Thermo Fisher Scientific), in 1% NGS in HMK for 1 hour followed by a wash with HMK four times. For DNA staining in fixed cells, DAPI (0.5 µg/ml) was added to the cells for 5 min followed by washing with HMK. The stained cells were embedded in PPDI.

Fluorescent microscopy on fixed samples

Image stacks of fixed cells were acquired by using Delta Vision Ultra (GE Healthcare) with an Olympus UPLXAPO 100× [numerical aperture (NA) 1.45] or UPLXAPO 60× (NA 1.42) objective. Optical sections at a thickness of 0.2 µm were imaged. For fig. S1D, images were deconvolved using SoftWoRx software (Applied Precision/GE Healthcare). For interphase nuclei, the best-focused section to the middle of nuclei was extracted after correcting the chromatic aberration. Image analysis was performed using Fiji/ImageJ.

To quantify the intranuclear signal intensity of Repli-Histo labeling, DAPI-stained nuclear regions were segmented on the basis of Huang's fuzzy thresholding method with Fiji/ImageJ, and the total nuclear pixel intensities (arb. unit) and mean nuclear intensities (arb. unit) for DAPI and all other signals of interest were measured. DNA content was plotted on the x axis using total DAPI intensities. The cell cycle profiles in Fig. 5A were estimated by the Dean-Jett-Fox method. At least 100 to 200 random interphase cells were imaged in all scatter plots. The colocalization of the EdU and the Repli-Histo signals was evaluated by the pixel-wise Pearson's correlation coefficient between each channel in the nuclear regions.

Single-nucleosome imaging microscopy

Established cell lines were cultured on poly-L-lysine-coated (P1524-500MG, Sigma-Aldrich) glass-based dishes (3970-035, Iwaki). H2B-HaloTag and H3.2-HaloTag molecules were fluorescently labeled with 50 pM HaloTag JF646 ligand or Repli-Histo labeled as described above.

Single-nucleosome imaging was performed as described previously (10, 31, 33, 36). To maintain cell culture conditions (37°C, 5% CO₂, and humidity) under the microscope, a live-cell chamber and a digital gas mixer (STXG-WSKMX-SET, Tokai Hit) were used. Single nucleosomes were observed by using an inverted Nikon Eclipse Ti2 microscope, an ILE 400 laser combiner (Andor) with 100-mW 561-nm and 140-mW 637-nm laser systems, and a scientific complementary metal-oxide semiconductor (sCMOS) ORCA-Fusion BT camera (C15440-20UP, Hamamatsu Photonics). Fluorescently labeled histones in living cells were excited by the 561/637-nm laser through an objective lens [100× PlanApo total internal reflection fluorescence (TIRF), NA 1.49; Nikon] and detected at 582 to 626/676 to 786 nm. An oblique illumination system with the TIRF unit (Nikon) was used to excite the labeled histone molecules within a limited thin area in the cell nucleus and reduce background noise. R110direct-labeled H3.2-Halo was imaged with light-emitting diode (LED) epillumination (X-Cite XYLIS, Excelitas Technologies) and detected at 503 to 547 nm. Sequential image frames were acquired using NIS elements software (AR v5.30.03 64bit, Nikon) at a frame rate of 50 ms under continuous illumination. The frame rate and exposure time were controlled using a NI-DAQ board (PCI3-6353, National Instruments). Dual-color imaging was performed through a beam splitter

W-VIEW GEMINI (Hamamatsu Photonics) detected at 573 to 613 nm (TMR) and 662 to 690 nm (JF646).

Chemical treatment

For single-nucleosome imaging on chemically fixed cells, cells grown on poly-L-lysine-coated glass-based dishes were incubated in 2% FA in 1× HBSS at 37°C for 15 min and washed with 1× HBSS three times. The following single-nucleosome imaging was performed as described above.

Single-nucleosome tracking analysis

The methods for image processing, single-molecule tracking, and single-nucleosome movement analysis were described previously (6). The background noise signals in the acquired sequential tiff images were subtracted with the rolling ball background subtraction (rolling ball radius: 50 pixels) using Fiji/ImageJ. The nuclear regions in the images were manually extracted. Following this step, the diffraction-limited fluorescent dots in each image were fitted to a Gaussian function to obtain the center of the distribution, and its trajectory was tracked with u-track [MATLAB package (57)]. To ascertain the position determination accuracy of the H3.2-HaloTag-nucleosomes in FA-fixed cells, distributions of nucleosome displacements from the centroids of the trajectories in the x and y planes ($n = 11$ or 12 molecules) were fitted to Gaussian functions. The calculated position determination accuracy in each experiment was described in figs. S4B, S11B, and S12B.

For single-nucleosome movement analysis, the displacement and MSD of the fluorescent dots were calculated on the basis of their trajectory using a Python script. The originally calculated MSD was in 2D. To obtain the 3D value, the 2D value was multiplied by 1.5 (4 to 6 Dt). The calculated MSDs were fitted as a subdiffusive model $MSD(t) = 6D \cdot t^\alpha$, where α is an anomalous diffusion exponent ($0 < \alpha < 1$). Statistical analyses of the obtained single-nucleosome MSD captured through each histone protein were performed using Python.

Two-point MSD analysis

For dual-color single nucleosome imaging, the HeLa cells were first arrested at G₁-S with a double thymidine block. One or 5 hours after the cells were released into a thymidine-free medium, the cells were incubated with 10 µM 7BRO for 60 min at 37°C in 5% CO₂ followed by a wash with medium without 7BRO three times. Subsequently, the cells were labeled with the mixture of 500 pM HaloTag TMR ligand and 10 nM JF646 ligand for 10 to 15 min.

Image processing, dot detection, and tracking of the dual-color single-nucleosome tracking images were carried out as described above. The calculated position determination accuracy through the beam splitter was 11.0 nm (TMR particles) and 10.4 nm (JF646 particles) (see fig. S11B). Positions of spots labeled by TMR and JF646 colors were corrected by second-order polynomial transformation. Parameters of the transformation were estimated based on the 0.1-µm TetraSpeck bead (T7279, Thermo Fisher Scientific) imaging and calculations were performed using the Python library Scikit image. To analyze the movements of two nucleosomes labeled with two colors (TMR and JF646), we picked closely located (<150 nm) pairs of TMR and JF646 trajectories from each image movie. Around 60 to 150 pairs of the dots were obtained from a single experiment. The two-point MSD of the fluorescent dots was calculated as described in (10, 67). In our single-nucleosome tracking, trajectories of TMR- and JF646-dots on the XY plane, $\{S_{\text{TMR}}(t_m)\}_{m=0}^{M-1}$ and $\{S_{\text{JF646}}(t_m)\}_{m=0}^{M-1}$

were simultaneously acquired, where the time interval was $\Delta t = 0.05$ s and $t_m = m \Delta t$ ($m = 0, 1, 2, \dots, M - 1$). To evaluate dynamic fluctuations between two points, we dealt with the relative vector between two trajectories, $\mathbf{Q}(t_m) = \mathbf{S}_{\text{TMR}}(t_m) - \mathbf{S}_{\text{JF646}}(t_m)$. Then, we calculated the two-point MSD for the lag time $t_n = n \Delta t$ by

$$\text{MSD}(t_n) = \left\langle \frac{1}{M-n} \sum_{m=0}^{M-1-n} [\mathbf{Q}(t_{m+n}) - \mathbf{Q}(t_m)]^2 \right\rangle_{t_n} \times \frac{3}{2} \quad (1)$$

where $\langle \cdot \rangle_{t_n}$ represents the ensemble average for trajectories at the lag time t_n and the coefficient $3/2$ is a correction factor for conversion from 2D to 3D values.

Segmentation of the class III chromatin regions

To extract the single-nucleosome trajectories colocalized with late-S replication foci (fig. S6A), we segmented the late-S replicated chromatin regions using dense TMR-labeled images. First, 10-frame (0.5 s) averaged TMR images were processed with an ImageJ band-pass filter function with the filtering of large structures down to 30 pixels and small structures up to 5 pixels. The filtered images were then binarized using Otsu's method. The two-pixel-dilated binary masks were defined as the late-S replication foci region. The detected JF646 dots located inside the foci regions were extracted on the basis of the centroids of their trajectories (i.e., time average of xy coordinates) as described previously (35). The categorized trajectories were used in subsequent analyses. For Fig. 4 (D and E), we also segmented the nucleolus-associated regions and the perinuclear regions of class II chromatin in the same way.

Angle distribution analysis

Angle distribution analysis was performed as described in (36). For the tracked consecutive points $\{(x_0, y_0), (x_1, y_1), \dots, (x_n, y_n), \dots\}$ of a single nucleosome on the xy plane, we converted the data into a set of displacement vectors, $\Delta \mathbf{r}_n = (x_{n+1} - x_n, y_{n+1} - y_n)^t$. Then, we calculated the angle between two vectors $\Delta \mathbf{r}_n$ and $\Delta \mathbf{r}_{n+1}$. We carried out this procedure for all the points of each trajectory in our experiments. We plotted the normalized polar histogram by our Python program (35). The angle distribution was normalized by 2π , and the values correspond to the probability density.

Monte Carlo simulation of nucleosomes and model proteins

We performed a Metropolis Monte Carlo method without long-range potential or hydrodynamic interactions to determine the diffusive motion of molecules (70). The diameter of the crowding agents used in this simulation was 9.6 nm, comparable to those of a single-nucleosome molecule determined by its volume (1). The diffusion coefficients (D s) of the crowding agents were $0.3 \mu\text{m}^2 \text{s}^{-1}$. The diameters of tracers were 10 to 20 nm. The D s of tracers were given as $90 \mu\text{m}^2 \text{s}^{-1}$ divided by its diameter in nanometers (9 to $4.5 \mu\text{m}^2 \text{s}^{-1}$). These D s were determined by the Stokes-Einstein relationship based on parameters from the EGFP monomer, the diameter and D of which were 3.8 nm and $23.5 \mu\text{m}^2 \text{s}^{-1}$, respectively (71). Simulations were conducted in a 298 nm-by-149 nm-by-149 nm cuboid with reflective and periodic boundaries on long and other axes, respectively. These boundary conditions avoid problems caused by finite space. The simulation space had two different crowding conditions, which corresponded to 11.5 mg/ml (uncrowded region) and 85.9 mg/ml (chromatin domain) densities (72). Ninety-six and 692 copies of

9.6-nm spheres (nucleosomes) were randomly placed in the left and right halves of the cuboid, respectively. The behavior of these crowding agents mimicked the diffusion of nucleosomes, which displaced less than a few nanometers (0 to 12 nm) from their initial positions [the “dog on a leash” model; see also (71, 73)]. In addition, the centers of crowding agents were restricted in each half to keep the initial concentration. Initially, 10 tracers were randomly placed in the left (uncrowded) region. These tracers were allowed to diffuse freely in the whole cuboidal space. The motion of the tracers and crowding agents was iteratively simulated following previously described procedures (71, 73). The simulation time step, Δt , was 10 ns. Simulations (100 ms) were run, recording the position of the tracers every 10 μs . To analyze the search in genomic regions by molecules, the first collision times were logged for all pairs of tracers and crowding agents. Fifty simulations (500 tracers in total) were performed for each condition. For the analysis of penetration kinetics, the time courses of the proportion of particles meeting the given conditions were fitted with an exponential function, $1 - e^{(-at-b)}$.

Supplementary Materials

The PDF file includes:

Figs. S1 to S13

Legends for movies S1 to S31

Other Supplementary Material for this manuscript includes the following:

Movies S1 to S31

REFERENCES AND NOTES

- K. Luger, A. W. Mader, R. K. Richmond, D. F. Sargent, T. J. Richmond, Crystal structure of the nucleosome core particle at 2.8 Å resolution. *Nature* **389**, 251–260 (1997).
- M. Koyama, H. Kurumizaka, Structural diversity of the nucleosome. *J. Biochem.* **163**, 85–95 (2018).
- T. Misteli, The self-organizing genome: Principles of genome architecture and function. *Cell* **183**, 28–45 (2020).
- K. Maeshima, S. Iida, S. Tamura, Physical nature of chromatin in the nucleus. *Cold Spring Harb. Perspect. Biol.* **13**, a040675 (2021).
- A. S. Belmont, K. Bruce, Visualization of G1 chromosomes: A folded, twisted, supercoiled chromonema model of interphase chromatid structure. *J. Cell Biol.* **127**, 287–302 (1994).
- T. Nozaki, R. Imai, M. Tanbo, R. Nagashima, S. Tamura, T. Tani, Y. Joti, M. Tomita, K. Hibino, M. T. Kanemaki, K. S. Wendt, Y. Okada, T. Nagai, K. Maeshima, Dynamic organization of chromatin domains revealed by super-resolution live-cell imaging. *Mol. Cell* **67**, 282–293. e7 (2017).
- B. Bintu, L. J. Mateo, J. H. Su, N. A. Sinnott-Armstrong, M. Parker, S. Kinrot, K. Yamaya, A. N. Boettiger, X. Zhuang, Super-resolution chromatin tracing reveals domains and cooperative interactions in single cells. *Science* **362**, eaau1783 (2018).
- E. Miron, R. Oldenkamp, J. M. Brown, D. M. S. Pinto, C. S. Xu, A. R. Faria, H. A. Shaban, J. D. P. Rhodes, C. Innocent, S. de Ornellas, H. F. Hess, V. Buckle, L. Schermelleh, Chromatin arranges in chains of mesoscale domains with nanoscale functional topography independent of cohesin. *Sci. Adv.* **6**, eaab8811 (2020).
- T. Cremer, M. Cremer, B. Hubner, A. Silahatoglu, M. Hendzel, C. Lanctot, H. Strickfaden, C. Cremer, The interchromatin compartment participates in the structural and functional organization of the cell nucleus. *Bioessays* **42**, e1900132 (2020).
- T. Nozaki, S. Shinkai, S. Ide, K. Higashi, S. Tamura, M. A. Shimazoe, M. Nakagawa, Y. Suzuki, Y. Okada, M. Sasai, S. Onami, K. Kurokawa, S. Iida, K. Maeshima, Condensed but liquid-like domain organization of active chromatin regions in living human cells. *Sci. Adv.* **9**, eadf1488 (2023).
- Y. Li, V. Agrawal, R. K. A. Virk, E. Roth, W. S. Li, A. Eshein, J. Frederick, K. Huang, L. Almssalha, R. Bleher, M. A. Carignano, I. Szleifer, V. P. Dravid, V. Backman, Analysis of three-dimensional chromatin packing domains by chromatin scanning transmission electron microscopy (ChromSTEM). *Sci. Rep.* **12**, 12198 (2022).
- K. Maeshima, S. Iida, M. A. Shimazoe, S. Tamura, S. Ide, Is euchromatin really open in the cell? *Trends Cell Biol.* **34**, 7–17 (2024).
- E. Lieberman-Aiden, N. L. van Berkum, L. Williams, M. Imakaev, T. Ragoczy, A. Telling, I. Amit, B. R. Lajoie, P. J. Sabo, M. O. Dorschner, R. Sandstrom, B. Bernstein, M. A. Bender, M. Groudine, A. Gnirke, J. Stamatoyannopoulos, L. A. Mirny, E. S. Lander, J. Dekker, Comprehensive mapping of long-range interactions reveals folding principles of the human genome. *Science* **326**, 289–293 (2009).

14. L. Mirny, J. Dekker, Mechanisms of chromosome folding and nuclear organization: Their interplay and open questions. *Cold Spring Harb. Perspect. Biol.* **14**, a040147 (2022).
15. S. S. Rao, M. H. Huntley, N. C. Durand, E. K. Stamenova, I. D. Bochkov, J. T. Robinson, A. L. Sanborn, I. Machol, A. D. Omer, E. S. Lander, E. L. Aiden, A 3D map of the human genome at kilobase resolution reveals principles of chromatin looping. *Cell* **159**, 1665–1680 (2014).
16. S. I. Grewal, S. Jia, Heterochromatin revisited. *Nat. Rev. Genet.* **8**, 35–46 (2007).
17. R. C. Allshire, H. D. Madhani, Ten principles of heterochromatin formation and function. *Nat. Rev. Mol. Cell Biol.* **19**, 229–244 (2018).
18. J. Padeken, S. P. Methot, S. M. Gasser, Establishment of H3K9-methylated heterochromatin and its functions in tissue differentiation and maintenance. *Nat. Rev. Mol. Cell Biol.* **23**, 623–640 (2022).
19. B. Alberts, R. Heald, A. Johnson, D. Morgan, M. Raff, K. Roberts, P. Walter, J. Wilson, T. Hunt, *Molecular Biology of the Cell* (W. W. Norton, ed. 7, 2022).
20. M. Gelleri, S. Y. Chen, B. Hubner, J. Neumann, O. Kroger, F. Sadlo, J. Imhoff, M. J. Hendzel, M. Cremer, T. Cremer, H. Strickfaden, C. Cremer, True-to-scale DNA-density maps correlate with major accessibility differences between active and inactive chromatin. *Cell Rep.* **42**, 112567 (2023).
21. S. Shinkai, T. Nozaki, K. Maeshima, Y. Togashi, Dynamic nucleosome movement provides structural information of topological chromatin domains in living human cells. *PLOS Comput. Biol.* **12**, e1005136 (2016).
22. H. A. Shaban, R. Barth, K. Bystricky, Formation of correlated chromatin domains at nanoscale dynamic resolution during transcription. *Nucleic Acids Res.* **46**, e77 (2018).
23. S. Uchino, Y. Ito, Y. Sato, T. Handa, Y. Ohkawa, M. Tokunaga, H. Kimura, Live imaging of transcription sites using an elongating RNA polymerase II-specific probe. *J. Cell Biol.* **221**, e202104134 (2022).
24. J. Lerner, P. A. Gomez-Garcia, R. L. Mc Carthy, Z. Liu, M. Lakadamyali, K. S. Zaret, Two-parameter mobility assessments discriminate diverse regulatory factor behaviors in chromatin. *Mol. Cell* **79**, 677–688.e6 (2020).
25. H. Kimura, P. R. Cook, Kinetics of core histones in living human cells: Little exchange of H3 and H4 and some rapid exchange of H2B. *J. Cell Biol.* **153**, 1341–1353 (2001).
26. P. Heun, T. Laroche, K. Shimada, P. Furrer, S. M. Gasser, Chromosome dynamics in the yeast interphase nucleus. *Science* **294**, 2181–2186 (2001).
27. V. Levi, Q. Ruan, M. Plutz, A. S. Belmont, E. Gratton, Chromatin dynamics in interphase cells revealed by tracking in a two-photon excitation microscope. *Biophys. J.* **89**, 4275–4285 (2005).
28. T. Germier, S. Kocanova, N. Walther, A. Bancaud, H. A. Shaban, H. Sellou, A. Z. Politi, J. Ellenberg, F. Gallardo, K. Bystricky, Real-time imaging of a single gene reveals transcription-initiated local confinement. *Biophys. J.* **113**, 1383–1394 (2017).
29. H. Ma, L. C. Tu, Y. C. Chung, A. Naseri, D. Grunwald, S. Zhang, T. Pederson, Cell cycle- and genomic distance-dependent dynamics of a discrete chromosomal region. *J. Cell Biol.* **218**, 1467–1477 (2019).
30. M. N. Saxton, T. Morisaki, D. Krapf, H. Kimura, T. J. Stasevich, Live-cell imaging uncovers the relationship between histone acetylation, transcription initiation, and nucleosome mobility. *Sci. Adv.* **9**, ead4819 (2023).
31. S. Ide, S. Tamura, K. Maeshima, Chromatin behavior in living cells: Lessons from single-nucleosome imaging and tracking. *Bioessays* **44**, e2200043 (2022).
32. M. Lakadamyali, Single nucleosome tracking to study chromatin plasticity. *Curr. Opin. Cell Biol.* **74**, 23–28 (2022).
33. A. Semeigazin, S. Iida, K. Minami, S. Tamura, S. Ide, K. Higashi, A. Toyoda, K. Kurokawa, K. Maeshima, Behaviors of nucleosomes with mutant histone H4s in euchromatic domains of living human cells. *Histochem. Cell Biol.* **162**, 23–40 (2024).
34. K. Wagh, D. A. Stavreva, R. A. M. Jensen, V. Paakinaho, G. Fettweis, R. L. Schiltz, D. Wustner, S. Mandrup, D. M. Presman, A. Upadhyaya, G. L. Hager, Dynamic switching of transcriptional regulators between two distinct low-mobility chromatin states. *Sci. Adv.* **9**, eade1122 (2023).
35. K. Hibino, Y. Sakai, S. Tamura, M. Takagi, K. Minami, T. Natsume, M. A. Shimazoe, M. T. Kanemaki, N. Imamoto, K. Maeshima, Single-nucleosome imaging unveils that condensins and nucleosome-nucleosome interactions differentially constrain chromatin to organize mitotic chromosomes. *Nat. Commun.* **15**, 7152 (2024).
36. S. Iida, S. Shinkai, Y. Itoh, S. Tamura, M. T. Kanemaki, S. Onami, K. Maeshima, Single-nucleosome imaging reveals steady-state motion of interphase chromatin in living human cells. *Sci. Adv.* **8**, eabn5626 (2022).
37. R. Nagashima, K. Hibino, S. S. Ashwin, M. Babokhov, S. Fujishiro, R. Imai, T. Nozaki, S. Tamura, T. Tani, H. Kimura, M. Shribak, M. T. Kanemaki, M. Sasaki, K. Maeshima, Single nucleosome imaging reveals loose genome chromatin networks via active RNA polymerase II. *J. Cell Biol.* **218**, 1511–1530 (2019).
38. A. E. Vouzas, D. M. Gilbert, Mammalian DNA replication timing. *Cold Spring Harb. Perspect. Biol.* **13**, a040162 (2021).
39. D. S. Dimitrova, B. Berezney, The spatio-temporal organization of DNA replication sites is identical in primary, immortalized and transformed mammalian cells. *J. Cell Sci.* **115**, 4037–4051 (2002).
40. V. O. Chagin, C. S. Casas-Delucchi, M. Reinhart, L. Schermelleh, Y. Markaki, A. Mäiser, J. J. Bolius, A. Bensimon, M. Fillies, P. Domaing, Y. M. Rozanov, H. Leonhardt, M. C. Cardoso, 4D Visualization of replication foci in mammalian cells corresponding to individual replicons. *Nat. Commun.* **7**, 11231 (2016).
41. S. Mendiratta, A. Gatto, G. Almouzni, Histone supply: Multitiered regulation ensures chromatin dynamics throughout the cell cycle. *J. Cell Biol.* **218**, 39–54 (2019).
42. K. Ahmad, S. Henikoff, The histone variant H3.3 marks active chromatin by replication-independent nucleosome assembly. *Mol. Cell* **9**, 1191–1200 (2002).
43. F. A. Ran, P. D. Hsu, J. Wright, V. Agarwala, D. A. Scott, F. Zhang, Genome engineering using the CRISPR-Cas9 system. *Nat. Protoc.* **8**, 2281–2308 (2013).
44. J. B. Grimm, B. P. English, J. Chen, J. P. Slaughter, Z. Zhang, A. Revyakin, R. Patel, J. J. Macklin, D. Normanno, R. H. Singer, T. Lionnet, L. D. Lavis, A general method to improve fluorophores for live-cell and single-molecule microscopy. *Nat. Methods* **12**, 244–250 (2015).
45. C. Clement, G. A. Orsi, A. Gatto, E. Boyarchuk, A. Forest, B. Hajj, J. Mine-Hattab, M. Garnier, Z. A. Gurard-Levin, J. P. Quivy, G. Almouzni, High-resolution visualization of H3 variants during replication reveals their controlled recycling. *Nat. Commun.* **9**, 3181 (2018).
46. R. A. Merrill, J. Song, R. A. Kephart, A. J. Klomp, C. E. Noack, S. Strack, A robust and economical pulse-chase protocol to measure the turnover of HaloTag fusion proteins. *J. Biol. Chem.* **294**, 16164–16171 (2019).
47. A. Gatto, A. Forest, J.-P. Quivy, G. Almouzni, HIRA-dependent boundaries between H3 variants shape early replication in mammals. *Mol. Cell* **82**, 1909–1923.e5 (2022).
48. ENCODE Project Consortium, An integrated encyclopedia of DNA elements in the human genome. *Nature* **489**, 57–74 (2012).
49. K. Xiong, J. Ma, Revealing Hi-C subcompartments by imputing inter-chromosomal chromatin interactions. *Nat. Commun.* **10**, 5069 (2019).
50. J. Zhang, D. Lee, V. Dhimani, P. Jiang, J. Xu, P. McGillivray, H. Yang, J. Liu, W. Meyerson, D. Clarke, M. Gu, S. Li, S. Lou, J. Xu, L. Lochovsky, M. Ung, L. Ma, S. Yu, Q. Cao, A. Harmanci, K. K. Yan, A. Sethi, G. Gürsoy, M. R. Schoenberg, J. Rozowsky, J. Warrell, P. Emani, Y. T. Yang, T. Galeev, X. Kong, S. Liu, X. Li, J. Krishnan, Y. Feng, J. C. Rivera-Mulia, J. Adrian, J. R. Broach, M. Bolt, J. Moran, D. Fitzgerald, V. Dileep, T. Liu, S. Mei, T. Sasaki, C. Trevilla-Garcia, S. Wang, Y. Wang, C. Zang, D. Wang, R. J. Klein, M. Snyder, D. M. Gilbert, K. Yip, C. Cheng, F. Yue, X. S. Liu, K. P. White, M. Gerstein, An integrative ENCODE resource for cancer genomics. *Nat. Commun.* **11**, 3696 (2020).
51. P. A. Zhao, T. Sasaki, D. M. Gilbert, High-resolution Repli-Seq defines the temporal choreography of initiation, elongation and termination of replication in mammalian cells. *Genome Biol.* **21**, 76 (2020).
52. C. Van Rechem, F. Ji, D. Chakraborty, J. C. Black, R. I. Sadreyev, J. R. Whetstone, Collective regulation of chromatin modifications predicts replication timing during cell cycle. *Cell Rep.* **37**, 109799 (2021).
53. E. G. Lund, I. Duband-Goulet, A. Oldenburg, B. Buendia, P. Collas, Distinct features of lamin A-interacting chromatin domains mapped by ChIP-sequencing from sonicated or micrococcal nuclease-digested chromatin. *Nucleus* **6**, 30–39 (2015).
54. M. Tokunaga, N. Imamoto, K. Sakata-Sogawa, Highly inclined thin illumination enables clear single-molecule imaging in cells. *Nat. Methods* **5**, 159–161 (2008).
55. E. Betzig, G. H. Patterson, R. Sougrat, O. W. Lindwasser, S. Olenych, J. S. Bonifacino, M. W. Davidson, J. Lippincott-Schwartz, H. F. Hess, Imaging intracellular fluorescent proteins at nanometer resolution. *Science* **313**, 1642–1645 (2006).
56. M. J. Rust, M. Bates, X. Zhuang, Sub-diffraction-limit imaging by stochastic optical reconstruction microscopy (STORM). *Nat. Methods* **3**, 793–795 (2006).
57. K. Jaqaman, D. Loerke, M. Mettlen, H. Kuwata, S. Grinstein, S. L. Schmid, G. Danuser, Robust single-particle tracking in live-cell time-lapse sequences. *Nat. Methods* **5**, 695–702 (2008).
58. I. Izeddin, V. Recamier, L. Bosanac, I. I. Cisse, L. Boudarene, C. Dugast-Darzacq, F. Proux, O. Benichou, R. Voituriez, O. Bensaude, M. Dahan, X. Darzacq, Single-molecule tracking in live cells reveals distinct target-search strategies of transcription factors in the nucleus. *eLife* **3**, e02230 (2014).
59. B. van Steensel, A. S. Belmont, Lamina-associated domains: Links with chromosome architecture, heterochromatin, and gene repression. *Cell* **169**, 780–791 (2017).
60. T. Peng, Y. Hou, H. Meng, Y. Cao, X. Wang, L. Jia, Q. Chen, Y. Zheng, Y. Sun, H. Chen, T. Li, C. Li, Mapping nucleolus-associated chromatin interactions using nucleolus Hi-C reveals pattern of heterochromatin interactions. *Nat. Commun.* **14**, 350 (2023).
61. C. A. Reznikoff, D. W. Brankow, C. Heidelberger, Establishment and characterization of a cloned line of C3H mouse embryo cells sensitive to postconfluence inhibition of division. *Cancer Res.* **33**, 3231–3238 (1973).
62. C. Maison, J. P. Quivy, A. V. Probst, G. Almouzni, Heterochromatin at mouse pericentromeres: A model for de novo heterochromatin formation and duplication during replication. *Cold Spring Harb. Symp. Quant. Biol.* **75**, 155–165 (2010).
63. S. Kubota, Y. Fukumoto, K. Ishibashi, S. Soeda, S. Kubota, R. Yuki, Y. Nakayama, K. Aoyama, N. Yamaguchi, N. Yamaguchi, Activation of the prereplication complex is blocked by mimosine through reactive oxygen species-activated ataxia telangiectasia mutated (ATM) protein without DNA damage. *J. Biol. Chem.* **289**, 5730–5746 (2014).

64. D. A. Jackson, A. Pombo, Replicon clusters are stable units of chromosome structure: Evidence that nuclear organization contributes to the efficient activation and propagation of S phase in human cells. *J. Cell Biol.* **140**, 1285–1295 (1998).
65. A. Costa, J. F. X. Diffley, The Initiation of Eukaryotic DNA replication. *Annu. Rev. Biochem.* **91**, 107–131 (2022).
66. H. Polasek-Sedlackova, T. C. R. Miller, J. Krejci, M. B. Rask, J. Lukas, Solving the MCM paradox by visualizing the scaffold of CMG helicase at active replisomes. *Nat. Commun.* **13**, 6090 (2022).
67. M. Gabriele, H. B. Brandao, S. Grosse-Holz, A. Jha, G. M. Dailey, C. Cattoglio, T. S. Hsieh, L. Mirny, C. Zechner, A. S. Hansen, Dynamics of CTCF- and cohesin-mediated chromatin looping revealed by live-cell imaging. *Science* **376**, 496–501 (2022).
68. S. Tanaka, R. Nakato, Y. Katou, K. Shirahige, H. Araki, Origin association of Sld3, Sld7, and Cdc45 proteins is a key step for determination of origin-firing timing. *Curr. Biol.* **21**, 2055–2063 (2011).
69. D. Mantiero, A. Mackenzie, A. Donaldson, P. Zegerman, Limiting replication initiation factors execute the temporal programme of origin firing in budding yeast. *EMBO J.* **30**, 4805–4814 (2011).
70. M. J. Morelli, P. R. ten Wolde, Reaction Brownian dynamics and the effect of spatial fluctuations on the gain of a push-pull network. *J. Chem. Phys.* **129**, 054112 (2008).
71. S. Hihara, C. G. Pack, K. Kaizu, T. Tani, T. Hanafusa, T. Nozaki, S. Takemoto, T. Yoshimi, H. Yokota, N. Imamoto, Y. Sako, M. Kinjo, K. Takahashi, T. Nagai, K. Maeshima, Local nucleosome dynamics facilitate chromatin accessibility in living mammalian cells. *Cell Rep.* **2**, 1645–1656 (2012).
72. R. Imai, T. Nozaki, T. Tani, K. Kaizu, K. Hibino, S. Ide, S. Tamura, K. Takahashi, M. Shribak, K. Maeshima, Density imaging of heterochromatin in live cells using orientation-independent-DIC microscopy. *Mol. Biol. Cell* **28**, 3349–3359 (2017).
73. K. Maeshima, K. Kaizu, S. Tamura, T. Nozaki, T. Kokubo, K. Takahashi, The physical size of transcription factors is key to transcriptional regulation in the chromatin domains. *J. Phys. Condens. Matter* **27**, 064116 (2015).
74. S. MacNeill, *The eukaryotic replisome: A guide to protein structure and function* (Springer, 2012).
75. I. Volpi, P. J. Gillespie, G. S. Chadha, J. J. Blow, The role of DDK and Treslin-MTBP in coordinating replication licensing and pre-initiation complex formation. *Open Biol.* **11**, 210121 (2021).
76. D. Cornacchia, V. Dileep, J. P. Quivy, R. Foti, F. Tili, R. Santarella-Mellwig, C. Antony, G. Almouzni, D. M. Gilbert, S. B. Buonomo, Mouse Rif1 is a key regulator of the replication-timing programme in mammalian cells. *EMBO J.* **31**, 3678–3690 (2012).
77. S. Yamazaki, A. Ishii, Y. Kanoh, M. Oda, Y. Nishito, H. Masai, Rif1 regulates the replication timing domains on the human genome. *EMBO J.* **31**, 3667–3677 (2012).
78. K. N. Klein, P. A. Zhao, X. Lyu, T. Sasaki, D. A. Bartlett, A. M. Singh, I. Tasan, M. Zhang, L. P. Watts, S. I. Hiraga, T. Natsume, X. Zhou, T. Baslan, D. Leung, M. T. Kanemaki, A. D. Donaldson, H. Zhao, S. Dalton, V. G. Corces, D. M. Gilbert, Replication timing maintains the global epigenetic state in human cells. *Science* **372**, 371–378 (2021).
79. G. J. Filion, J. G. van Bommel, U. Braunschweig, W. Talhout, J. Kind, L. D. Ward, W. Brugman, I. de Castro Genebra de Jesus, R. M. Kerkhoven, H. J. Bussemaker, B. van Steensel, Systematic protein location mapping reveals five principal chromatin types in *Drosophila* cells. *Cell* **143**, 212–224 (2010).
80. W. Wang, K. N. Klein, K. Proesmans, H. Yang, C. Marchal, X. Zhu, T. Borrmann, A. Hastie, Z. Weng, J. Bechhoefer, C. L. Chen, D. M. Gilbert, N. Rhind, Genome-wide mapping of human DNA replication by optical replication mapping supports a stochastic model of eukaryotic replication. *Mol. Cell* **81**, 2975–2988.e6 (2021).
81. D. J. Massey, A. Koren, High-throughput analysis of single human cells reveals the complex nature of DNA replication timing control. *Nat. Commun.* **13**, 2402 (2022).
82. S. Gnan, J. M. Josephides, X. Wu, M. Spagnuolo, D. Saulebekova, M. Bohec, M. Dumont, L. G. Baudrin, D. Fachinetti, S. Baulande, C. L. Chen, Kronos scRT: A uniform framework for single-cell replication timing analysis. *Nat. Commun.* **13**, 2329 (2022).
83. J. Bechhoefer, N. Rhind, Replication timing and its emergence from stochastic processes. *Trends Genet.* **28**, 374–381 (2012).
84. C. S. Casas-Delucchi, J. G. van Bommel, S. Haase, H. D. Herce, D. Nowak, D. Meilinger, J. H. Stear, H. Leonhardt, M. C. Cardoso, Histone hypoacetylation is required to maintain late replication timing of constitutive heterochromatin. *Nucleic Acids Res.* **40**, 159–169 (2012).
85. R. Foti, S. Gnan, D. Cornacchia, V. Dileep, A. Bulut-Karslioglu, S. Diehl, A. Buness, F. A. Klein, W. Huber, E. Johnstone, R. Loos, P. Bertone, D. M. Gilbert, T. Manke, T. Jenuwein, S. C. Buonomo, Nuclear architecture organized by Rif1 underpins the replication-timing program. *Mol. Cell* **61**, 260–273 (2016).
86. J. Sima, A. Chakraborty, V. Dileep, M. Michalski, K. N. Klein, N. P. Holcomb, J. L. Turner, M. T. Paulsen, J. C. Rivera-Mulia, C. Trevilla-Garcia, D. A. Bartlett, P. A. Zhao, B. K. Washburn, E. P. Nora, K. Kraft, S. Mundlos, B. G. Bruneau, M. Ljungman, P. Fraser, F. Ay, D. M. Gilbert, Identifying cis elements for spatiotemporal control of mammalian DNA replication. *Cell* **176**, 816–830.e18 (2019).
87. J. Brustel, N. Kirstein, F. Izard, C. Grimaud, P. Prorok, C. Cayrou, G. Schotta, A. F. Abdelsamie, J. Dejjardin, M. Mechali, G. Baldacci, C. Sardet, J. C. Cadoret, A. Schepers, E. Julien, Histone H4K20 tri-methylation at late-firing origins ensures timely heterochromatin replication. *EMBO J.* **36**, 2726–2741 (2017).
88. K. S. Heinz, C. S. Casas-Delucchi, T. Torok, D. Cmarko, A. Rapp, I. Raska, M. C. Cardoso, Peripheral re-localization of constitutive heterochromatin advances its replication timing and impairs maintenance of silencing marks. *Nucleic Acids Res.* **46**, 6112–6128 (2018).
89. S. I. Hiraga, T. Ly, J. Garzon, Z. Horejsi, Y. N. Ohkubo, A. Endo, C. Obuse, S. J. Boulton, A. I. Lamond, A. D. Donaldson, Human RIF1 and protein phosphatase 1 stimulate DNA replication origin licensing but suppress origin activation. *EMBO Rep.* **18**, 403–419 (2017).
90. D. P. Hoffman, G. Shtengel, C. S. Xu, K. R. Campbell, M. Freeman, L. Wang, D. E. Milkie, H. A. Pasolli, N. Iyer, J. A. Bogovic, D. R. Stabley, A. Shirinifard, S. Pang, D. Peale, K. Schaefer, W. Pomp, C. L. Chang, J. Lippincott-Schwartz, T. Kirchhausen, D. J. Solecki, E. Betzig, H. F. Hess, Correlative three-dimensional super-resolution and block-face electron microscopy of whole vitreously frozen cells. *Science* **367**, eaaz5357 (2020).
91. S. Iida, S. Ide, S. Tamura, M. Sasai, T. Tani, T. Goto, M. Shribak, K. Maeshima, Orientation-independent-DIC imaging reveals that a transient rise in depletion attraction contributes to mitotic chromosome condensation. *Proc. Natl. Acad. Sci. U.S.A.* **121**, e2403153121 (2024).
92. S. Ide, R. Imai, H. Ochi, K. Maeshima, Transcriptional suppression of ribosomal DNA with phase separation. *Sci. Adv.* **6**, eabb5953 (2020).
93. K. Labun, T. G. Montague, M. Krause, Y. N. Torres Cleuren, H. Tjeldnes, E. Valen, CHOPCHOP v3: Expanding the CRISPR web toolbox beyond genome editing. *Nucleic Acids Res.* **47**, W171–W174 (2019).
94. Y. Saito, J. Kobayashi, M. T. Kanemaki, K. Komatsu, RIF1 controls replication initiation and homologous recombination repair in a radiation dose-dependent manner. *J. Cell Sci.* **133**, jcs240036 (2020).
95. S. Ide, A. Sasaki, Y. Kawamoto, T. Bando, H. Sugiyama, K. Maeshima, Telomere-specific chromatin capture using a pyrrole-imidazole polyamide probe for the identification of proteins and non-coding RNAs. *Epigenetics Chromatin* **14**, 46 (2021).
96. P. A. Ewels, A. Peltzer, S. Fillinger, H. Patel, J. Alneberg, A. Wilm, M. U. Garcia, P. Di Tommaso, S. Nahnsen, The nf-core framework for community-curated bioinformatics pipelines. *Nat. Biotechnol.* **38**, 276–278 (2020).
97. Y. Zhang, T. Liu, C. A. Meyer, J. Eeckhoutte, D. S. Johnson, B. E. Bernstein, C. Nusbaum, R. M. Myers, M. Brown, W. Li, X. S. Liu, Model-based analysis of ChIP-Seq (MACS). *Genome Biol.* **9**, R137 (2008).
98. C. A. Davis, B. C. Hitz, C. A. Sloan, E. T. Chan, J. M. Davidson, I. Gabdank, J. A. Hilton, K. Jain, U. K. Baymuradov, A. K. Narayanan, K. C. Onate, K. Graham, S. R. Miyasato, T. R. Dreszer, J. S. Strattan, O. Jolanki, F. Y. Tanaka, J. M. Cherry, The Encyclopedia of DNA elements (ENCODE): Data portal update. *Nucleic Acids Res.* **46**, D794–D801 (2018).

Acknowledgments: We are grateful to K. M. Marshall for critical reading and editing of this manuscript, K. Sato for establishing a H3.2-Halo-expressing cell line, M. T. Kanemaki for providing HCT116 cells, and M. J. Hendzel for providing 10T1/2 cells. We thank H. Araki, K. Asakawa, S. Iida, and M. A. Shimazoe for the critical comments on this manuscript and helpful discussion. We also thank H. Masai, Y. Saito, K. Hibino, M. T. Kanemaki, Y. Shimamoto, T. Torisawa, H. Niki, and Maeshima Laboratory members for the helpful discussions and support. **Funding:** This work was supported by the Japan Society for the Promotion of Science (JSPS) and MEXT KAKENHI grants [JP20H05936, JP21H02453, JP23K17398, JP22H04925 (PAGS), and JP24H00061 to K.Ma. and 21H02535 and JP22H05606 to S.I.] and Takeda Science Foundation to K.Ma. K.Mi. was a SOKENDAI Special Researcher (JST SPRING JPMJSP2104) and is a JSPS Fellow (JP23KJ0998). **Author contributions:** Conceptualization: K.Mi. and K.Ma. Methodology: K.Mi., K.Ka., K.Ku., and K.Ma. Software: K.Mi., K.Ka., and K.Ku. Validation: K.Mi., K.N., A.T., and K.Ma. Formal analysis: K.Mi., K.Ka., K.H., A.T., and K.Ku. Investigation: K.Mi., K.N., S.T., A.T., and K.Ma. Resources: S.I., K.Mi., A.T., and K.Ku. Data curation: K.Mi., A.T., and K.Ku. Writing—original draft: K.Mi. and K.Ma. Writing—review and editing: K.Mi., K.Ma., K.Ka., K.Ku., and A.T. Visualization: K.Mi., K.N., S.T., K.H., A.T., and K.Ma. Supervision: K.T., A.T., and K.Ma. Project administration: A.T., K.Ku., and K.Ma. Funding acquisition: K.Mi., S.I., A.T., K.T., K.Ku., and K.Ma. **Competing interests:** The authors declare that they have no competing interests. **Data and materials availability:** All data needed to evaluate the conclusions in the paper are present in the paper and/or the Supplementary Materials. The genomics data have been deposited with links to BioProject accession number PRJDB19038 in the DDBJ BioProject database. The numerical code in the chromatin simulation is publicly available at <https://doi.org/10.5281/zenodo.13958856>. The scripts for track-sorting and angle-distribution analysis are available at <https://zenodo.org/records/12672197>.

Submitted 23 November 2024

Accepted 25 February 2025

Published 28 March 2025

10.1126/sciadv.adu8400